Viscoelastic and Dielectric Relaxation of a Cayley-Tree-Type Polyisoprene: Test of Molecular Picture of Dynamic Tube Dilation

H. Watanabe* and Y. Matsumiya

Institute for Chemical Research, Kyoto University, Uji, Kyoto 611-0011, Japan

E. van Ruymbeke and D. Vlassopoulos

Institute of Electronic Structure & Laser, FORTH, and Department of Materials Science & Technology, University of Crete, Heraklion 71110, Crete, Greece

N. Hadjichristidis

Department of Chemistry, University of Athens, Athens 15771, Greece

Received March 5, 2008; Revised Manuscript Received June 7, 2008

ABSTRACT: For an entangled Cayley-tree-type *cis*-polyisoprene (CT-PI) composed of two classes of arms, trifunctionally branched inner arms each carrying two outer arms ($M_i = 24.7 \times 10^3$ and $M_o = 12.3 \times 10^3$ for each inner and outer arm, respectively), the molecular picture of dynamic tube dilation (DTD) was examined through viscoelastic and dielectric data. The global motion of the arms was dielectrically active because they had the so-called type A dipole parallel along their backbone. The dielectric relaxation function $\Phi(t)$ thus measured for CT-PI enabled us to experimentally evaluate the survival fraction of the dilated tube $\varphi'(t)$, a key quantity in the DTD picture. In the conventional picture of *full-DTD*, relaxed portions of the arms are regarded as a simple solvent, thereby allowing the number of mutually equilibrated entanglement segments per dilated segment, $\beta(t)$, to fully increase to that in a corresponding solution, $\beta_{\text{f-DTD}}(t) = \{\varphi'(t)\}^{-d}$ with $d = 1.3$ for PI. The corresponding full-DTD relationship between $\varphi'(t)$ and the normalized viscoelastic relaxation function $\mu(t)$, $\mu_{\text{f-DTD}}(t) = \{\varphi'(t)\}^{1+d}$, did not hold for the $\varphi'(t)$ and $\mu(t)$ data of CT-PI. In contrast, in the molecular picture of *partial-DTD*, $\beta(t)$ is determined through competition of the constraint release (CR) motion of the focused chain and the motion of surrounding chains, the former determining the maximum possible $\beta_{\text{CR}}(t)$ value in a given time scale, t. In this picture, the length and time scales are consistently coarse-grained on the basis of the CR mechanism. The partial-DTD relationship, $\mu_{\text{p-DTD}}(t) = \varphi'(t)/\beta^*(t)$ with $\beta^*(t) = \min[\beta_{\text{f-DTD}}(t), \beta_{\text{CR}}(t)]$, was found to hold for the $\varphi'(t)$ and $\mu(t)$ data satisfactorily. In addition, analysis of the $\varphi'(t)$ data unequivocally indicated that the inner arm hardly relaxed until the outer arm relaxation completed; i.e., the hierarchical relaxation occurred *through partial-DTD*. These results suggested the importance of the consistent coarse graining in molecular description of the dynamics of branched chains in general.

1. Introduction

The entanglement in concentrated systems of long, flexible chains reflects the topological constraint due to uncrossability of the chains. This constraint vanishes when one of the mutually entangled chains exhibits large-scale (global) motion. In the tube model representing the constraint as a tube surrounding the chain, this transient nature of entanglement has been considered through the constraint release (CR) mechanism that activates changes of the tube shape.[1–4] The chain motion in long time scales is determined by competition between CR and other mechanisms such as reptation (for linear chains) and deep arm retraction (for star-branched chains).[2–4] Detailed description of this competition often results in an analytically intractable time evolution equation for the chain conformation,[5] although it may be managed through numerical methods.[5–8] This nonanalytical feature may be avoided if the motional unit considered in this equation, the entanglement segment of the molecular weight M_e and the size a (= tube diameter), is allowed to enlarge with time, as explained below.

The entanglement segment exhibits lateral, wriggling motion due to CR, but this motion is limited within an effective tube of a diameter $a'(t) > a$. In general, $a'(t)$ is determined by the number of local CR hopping[2] in a given time scale t and thus increases with increasing t; i.e., the effective tube *dilates* with t. Then, successive β entanglement segments with $\beta(t) = \{a'(t)/a\}^2$ are mutually equilibrated through the wriggling CR motion and can be coarse-grained into a larger, dilated segment of the size $a'(t)$.[3,4] This dilated segment does not exhibit lateral motion out of the dilated tube, and thus its motion occurs only along the axis of this tube, which greatly simplifies the description of the time evolution of the chain conformation (although some details of the CR motion may be smeared in the coarse-graining operation).

The above molecular picture of coarse-graining, *referred* to as dynamic tube dilation[3,4] (DTD), leads to a simple expression of linear viscoelastic quantities. For example, for monodisperse chains subjected to a small step strain at time 0, the normalized viscoelastic relaxation function, $\mu(t) = G(t)/G_N$ ($G(t)$ = relaxation modulus and G_N = entanglement plateau modulus), is written as[9,10]

$$\mu(t) = \frac{\varphi'(t)}{\beta(t)} \quad \text{with } \beta(t) = \{a'(t)/a\}^2 \tag{1}$$

Here, $\varphi'(t)$ is a tube survival fraction defined as the fraction of the entanglement segments that remain in a portion of the dilated tube preserving its initial configuration.

Equation 1 can be further simplified *if* the CR motion is sufficiently fast to allow the entanglement segments to fully explore, in the given time scale t, an entanglement mesh formed only by the surviving segments (having the fraction $\varphi'(t)$). For

* To whom all correspondence should be addressed. E-mail: hiroshi@scl.kyoto-u.ac.jp.

10.1021/ma800503e CCC: $40.75
Published on Web 08/02/2008

this case referred to as *full-DTD*, the relaxed portion can be regarded as a simple solvent so that $\beta(t)$ *fully* increases to that in the corresponding solution having a polymer concentration $\varphi'(t)$:[3,4,11–14] $\beta_{\text{f-DTD}}(t) = \{\varphi'(t)\}^{-d}$ with d being the dilation exponent ($d = 1-1.3$). Then, eq 1 reduces to the full-DTD relationship (frequently utilized in molecular models[12–14] though in somewhat different forms)

$$\mu_{\text{f-DTD}}(t) = \{\varphi'(t)\}^{1+d} \quad (a'(t) = a\{\varphi'(t)\}^{-d/2}) \tag{2}$$

However, if the CR motion is slow, the entanglement segments cannot always explore the whole entanglement mesh of the size $a\{\varphi'(t)\}^{-d/2}$ in time. For this case, $\beta(t)$ increases only up to the maximum possible number $\beta_{\text{CR}}(t)$ of the entanglement segments that can be mutually CR-equilibrated in the given time scale t.[9,10] Then, eq 1 can be rewritten in a general form of *partial-DTD*[9,10]

$$\mu_{\text{p-DTD}}(t) = \frac{\varphi'(t)}{\beta^*(t)} \quad \text{with } \beta^*(t) = \min[\beta_{\text{CR}}(t), \beta_{\text{f-DTD}}(t)] \tag{3}$$

Equation 3 reduces to eq 2 when $\beta_{\text{CR}}(t) \geq \beta_{\text{f-DTD}}(t)$.

As noted from eqs 2 and 3, the survival fraction of the dilated tube, $\varphi'(t)$, is the key quantity in the DTD molecular picture. For chains having so-called type A dipoles parallel along the backbone, $\varphi'(t)$ can be empirically evaluated from the dielectric data. Considering this feature, we recently conducted dielectric and viscoelastic measurements for *cis*-polyisoprene (PI) having the type A dipoles, evaluated $\varphi'(t)$ dielectrically, and examined the full- and partial-DTD relationships (eqs 2 and 3) for the viscoelastic $\mu(t)$ data. Equation 2 was found to hold satisfactorily for monodisperse linear PI.[15,16] In contrast, eq 2 failed but eq 3 held for monodisperse star-branched PI[10,16–18] and binary blends of long and short linear PI's.[9,11] The failure/validity of eq 2 can be related to a distribution of fast motional modes of the entanglement segments:[10] The monodisperse star PI as well as PI/PI blends have intensive fast modes that decrease $\varphi'(t)$ significantly at short t. Then, the chain cannot explore, in time, the largely dilated entanglement mesh considered in the full-DTD picture (eq 2), which naturally results in the failure of this picture. In contrast, the monodisperse linear PI has much less intensive fast modes. For this case, $\varphi'(t)$ decays only moderately at short t, thereby allowing the chain to fully explore the moderately dilated mesh and obey this picture.

The arm of the star-branched chain is considered to relax hierarchically from portions near the free end toward those near the branching point.[3,4,13,14] This hierarchical relaxation naturally enriches the fast motional modes of the entanglement segments and leads to the failure of the full-DTD picture. In relation to this point, we note that the relaxation of more complicatedly multibranched chains such as comb,[19–21] H-shape/pom-pom,[22–26] hyperbranch,[27] and dendritic Cayley-tree-type[28,29] chains exhibit an interbranch hierarchy (relaxation from outer branches to inner ones) in addition to the starlike intrabranch hierarchy. We expect that the full-DTD picture fails also for these multibranched chains because of their intensive fast modes resulting from the hierarchical relaxation. We can examine this expectation by testing molecular models incorporating the partial-DTD mechanism (or a related mechanism such as the relaxation in supertube) against different types of dynamic data, e.g., viscoelastic and diffusion data.[30] For example, the models proposed by van Ruymbeke et al.[29] and Larson et al.[31] can be utilized in this test. However, it is also important to test the expectation in an experimental way without fully relying on particular molecular models formulated on the basis of several delicate/detailed assumptions.

This paper attempts to make this *experimental* test with a strategy of minimizing the reliance on such delicate/detailed model assumptions. Following this strategy, we examined the slow dynamics of an entangled Cayley-tree-type PI (CT-PI) by comparing its dielectric and viscoelastic data. These data demonstrated the failure and validity of the full- and partial-DTD pictures, respectively, as expected. Details of the results are presented in this paper.

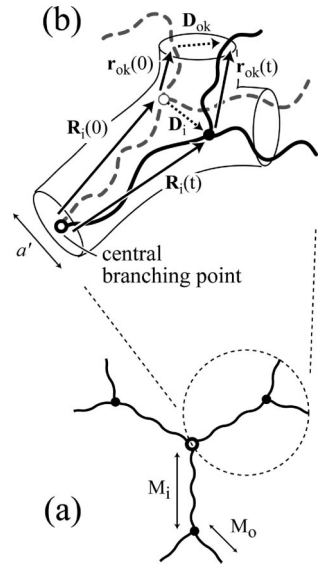

Figure 1. Schematic illustration of Cayley-tree-like PI (CT-PI).

2. Experimental Section

2.1. Material. The second generation (G-2) dendritic Cayley-tree-type polyisoprene (CT-PI) of high *cis* content (*cis*-1,4: 70%; *trans*-1,4: 23%; 3,4: 7%; determined from ^{1}H and ^{13}C NMR in $CDCl_3$) was synthesized by following the procedure described in a previous paper.[32] This CT-PI, having the molecular weight of $M = 14.8 \times 10^4$, was composed of two classes of arms, the inner and outer arms with molecular weights $M_i = 24.7 \times 10^3$ and $M_o = 12.3 \times 10^3$, respectively, as shown schematically in Figure 1a (bottom part). The polydispersity indices were $M_w/M_n = 1.05$ the CT-PI chain as a whole, $M_w/M_n = 1.04$ for the outer arm, and $M_w/M_n = 1.05$ for the inner arm combined with two outer arms (3-arm star PI precursor described in the synthetic step 3 below). Since the inner arm was polymerized from the anionic dimer of the outer arms (cf. steps 3 and 4) and not recovered in the isolated form, its polydispersity could not be determined experimentally. However, because of the similarity of chemistry for the polymerization steps for the outer and inner arms, the inner arm should have the polydispersity similar to that of the outer arm ($M_w/M_n = 1.04$).

Each inner arm ended in two end-grafted outer arms (cf. Figure 1a). This bifurcated structure and the M_i/M_o ratio being very close to 2 played an essential role in the Rouse-CR eigenmode analysis explained later. A pair of inner and outer arms had the molecular weight $M_i + M_o = 37.0 \times 10^3$ and were well entangled as a whole (cf. $M_e = 5 \times 10^3$ for PI[33]).

The synthesis of the CT-PI sample was performed in benzene at 25 °C with *sec*-butyllithium (*sec*-BuLi) and other compounds through the following steps:[32] (1) selective reaction of a PI living chain ($M_n = 12.3 \times 10^3$ determined from membrane osmometry (MO) in toluene at 37 °C, $M_w/M_n = 1.04$ determined from size exclusion chromatography (SEC) in tetrahydrofuran (THF)) with the chlorosilane group of 4-(chlorodimethylsilyl)styrene, a dual-functionality compound, to produce a styrenic PI macromonomer; this PI became the outer arm of CT-PI, (2) addition of a second living PI chain with identical M_n (outer arm equivalent to that in step 1) to the double bond of the macromonomer, (3) polymerization of isoprene with the anionic sites (styrenyllithium sites) to produce a living 3-arm star PI precursor ($M_n = 46.8 \times 10^3$ and $M_w = 49.3 \times 10^3$ determined from MO in toluene at 37 °C and low-angle laser light scattering (LALLS) in THF at 25 °C, respectively), and

(4) coupling reaction of the produced living star precursor with trichloromethylsilane to afford the G-2 CT-PI. The pure CT-PI sample, recovered after thorough fractionation from a solvent/nonsolvent (toluene/methanol) mixture, had molecular characteristics: $M_n = 14.0 \times 10^4$ (from MO in toluene at 37 °C), $M_w = 14.8 \times 10^4$ (from LALLS in THF at 25 °C), and the polydispersity index = 1.05 (from SEC in THF at 25 °C). The combined characterization results confirm the high molecular and compositional homogeneity of the G-2 dendritic polymer synthesized: The inner arm molecular weight was evaluated from the molecular weights of the outer arm and CT-PI as a whole; $M_i = (14.8 \times 10^4)/3 - 2 \times (12.3 \times 10^3) = 24.7 \times 10^3$. This M_i value agreed very well with that evaluated for the intermediate product, the 3-arm star PI, $M_i' = 49.3 \times 10^3 - 2 \times (12.3 \times 10^3)$, which reflected the high molecular and compositional homogeneity of the polymer.

Previously examined CT-PB samples appeared to have some small architectural dispersity (less than 15%).[29] This might have been the case also for our CT-PI sample, although this dispersity was not determined experimentally (the determination required a sophisticated technique such as the liquid chromatography at a critical condition). However, the above agreement of M_i and M_i' values suggests that the architectural dispersity of the CT-PI sample was small and did not influence significantly the data and results of analysis presented in this paper.

The high *cis* content PI chains anionically polymerized with lithium counter cation in benzene have so-called type A dipoles parallel along the backbone.[15–18] As noted from the above route of synthesis, the outer arms of CT-PI had the dipoles converging to their junction point (on the 4-(dimethylsilyl)styrenyl unit), and the inner arm had the dipoles starting from this point toward the central branching point (on the methylsilyl unit). The dielectric relaxation function of the CT-PI chain can be related to the chain conformation according to this dipole alignment. This relationship is later formulated on the basis of the conformation illustrated in Figure 1b (top part).

2.2. Measurements. For the CT-PI sample in the bulk state, dynamic viscoelastic measurements were conducted with a laboratory rheometer (ARES, Rheometrics; currently TA) in a cone−plate geometry of the gap angle = 0.1 rad and diameter = 2.5 cm. The strain amplitude γ_0 was kept small (≤ 0.1) in order to ensure the linearity of the storage and loss moduli, $G'(\omega)$ and $G''(\omega)$, measured as functions of the angular frequency ω. The time−temperature superposition was valid for the G' and G'' data measured at temperatures between −25 and 50 °C, and the data were reduced at a reference temperature, $T_r = 40$ °C. The shift factor was in agreement with that of linear PI samples reported previously.[11]

Since the CT-PI chain had the type A dipoles parallel along the arms, its global (large-scale) motion was dielectrically active. The dynamic dielectric constant $\varepsilon'(\omega)$ and dielectric loss $\varepsilon''(\omega)$ were measured at temperatures between 18 and 60 °C with the transformer bridge (TB) method utilizing a high accuracy capacitance bridge (1620A, Quad-Tech) and with the adsorption current (AdC) method utilizing a homemade circuit. Details of this circuit and AdC method (measurement of current under a rectangular voltage) were described elsewhere.[16] The time−temperature superposition was valid for the ε' and ε'' data, and the data were reduced at $T_r = 40$ °C. The shift factor a_T for this superposition agreed with that for the viscoelastic data, confirming that the dielectric and viscoelastic responses commonly reflected the global motion of the CT-PI chain.

3. Results and Discussion

3.1. Overview of Viscoelastic and Dielectric Behavior of CT-PI. Figure 2 shows the linear viscoelastic $G'(\omega)$ and $G''(\omega)$ data of the CT-PI sample at 40 °C. For convenience of later discussion, the data of loss tangent, $\tan\delta$ ($= G''/G'$), are also shown. Figure 3 shows the dielectric data, $\varepsilon_0 - \varepsilon'(\omega)$ with $\varepsilon_0 = \varepsilon'(0)$ (static dielectric constant) and $\varepsilon''(\omega)$, at the same T. Applying the previously reported iteration method[16] to the data in Figures 2 and 3, we evaluated the viscoelastic and dielectric

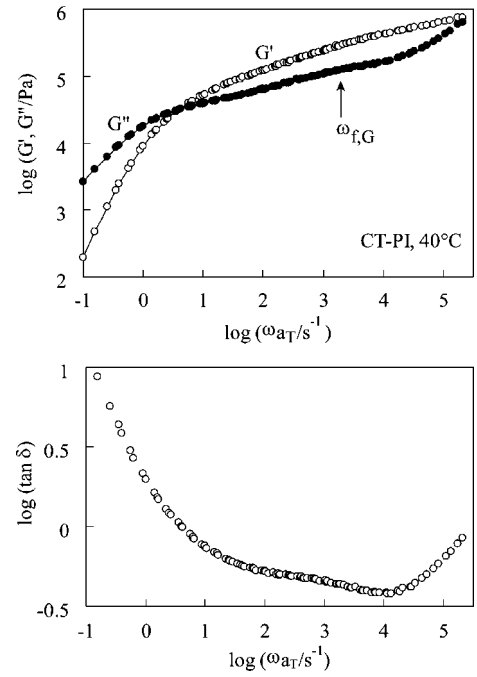

Figure 2. Storage and loss moduli, $G'(\omega)$ and $G''(\omega)$, and loss tangent, $\tan\delta(\omega)$, of CT-PI at 40 °C. These data are double-logarithmically plotted against angular frequency ω.

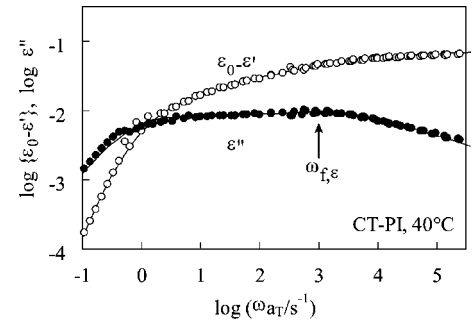

Figure 3. Decrease of dynamic dielectric constant, $\varepsilon_0 - \varepsilon'(\omega)$, and dielectric loss, $\varepsilon''(\omega)$, of CT-PI at 40 °C. These data are double-logarithmically plotted against angular frequency ω.

spectra, $\{h_p,\tau_{p,G}\}$ and $\{g_p,\tau_{p,\varepsilon}\}$ with $\tau_{p,G}$ and $\tau_{p,\varepsilon}$ being the relaxation times of pth viscoelastic and dielectric modes and h_p and g_p being the intensities of these modes. Both of $\tau_{p,G}$ and $\tau_{p,\varepsilon}$ were chosen to be in a range of $\tau_p \geq 3 \times 10^{-6}$ s (corresponding to the ω range in Figures 2 and 3) and have a logarithmic interval of 0.1, i.e., $\log \tau_{p,G}/\tau_{p+1,G} = \log \tau_{p,\varepsilon}/\tau_{p+1,\varepsilon} = 0.1$. The solid curves in the respective figures indicate G', G'', $\varepsilon_0 - \varepsilon'$, and ε'' recalculated from these spectra

$$G'(\omega) + iG''(\omega) = \sum_{p\geq 1} h_p \frac{i\omega\tau_{p,G}}{1 + i\omega\tau_{p,G}} \quad (i = \sqrt{-1}) \tag{4a}$$

$$\{\varepsilon_0 - \varepsilon'(\omega)\} + i\varepsilon''(\omega) = \sum_{p\geq 1} g_p \frac{i\omega\tau_{p,\varepsilon}}{1 + i\omega\tau_{p,\varepsilon}} \tag{4b}$$

The normalized viscoelastic and dielectric relaxation functions corresponding to the spectra, $\mu(t)$ and $\Phi(t)$, are shown in Figures 4 and 5 with circles. The curves in Figure 4 and the symbols other than the circle in Figure 5, respectively, indicate $\mu_{DTD}(t)$ for the DTD process and the survival fraction of the dilated tube, as explained later in more detail. The $\mu(t)$ and $\Phi(t)$ data (circles) are later utilized in our quantitative tests of the DTD molecular picture.

Some comments need to be made for the evaluation of the $\mu(t)$ and $\Phi(t)$ data. The DTD picture is formulated for the

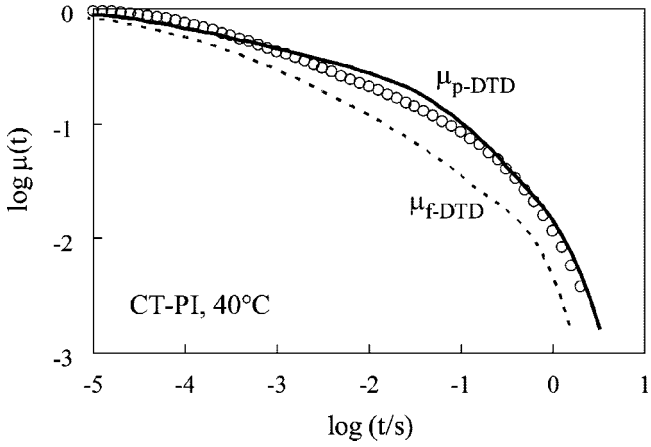

Figure 4. Normalized viscoelastic relaxation function $\mu(t)$ of CT-PI at 40 °C (circles). $\mu(t)$ was obtained from the $G'(\omega)$ and $G''(\omega)$ data shown in Figure 2. Dotted and solid curves indicate $\mu_{\text{f-DTD}}(t)$ and $\mu_{\text{p-DTD}}(t)$ for the cases of full- and partial-DTD, respectively. These $\mu_{\text{f-DTD}}(t)$ and $\mu_{\text{p-DTD}}(t)$ were evaluated from $\varphi'(t)$ shown in Figure 5. For further details, see text.

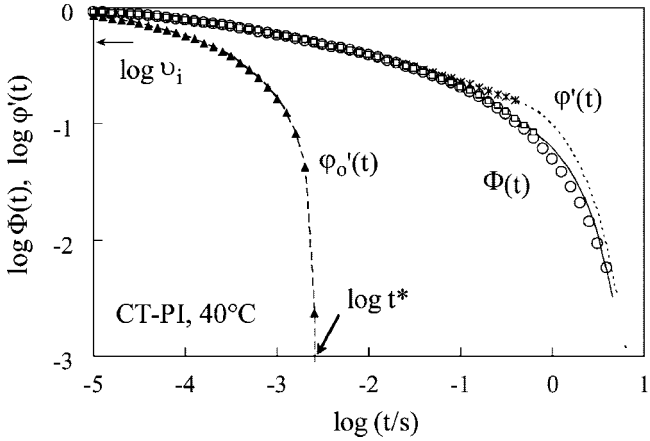

Figure 5. Normalized dielectric relaxation function $\Phi(t)$ of CT-PI at 40 °C (circles). $\Phi(t)$ was obtained from the $\varepsilon_0 - \varepsilon'(\omega)$ and $\varepsilon''(\omega)$ data shown in Figure 3. Asterisks connected by the dotted curve indicate the survival fraction of the dilated tube $\varphi'(t)$ evaluated for the case of full-DTD. Small squares connected by the solid curve show $\varphi'(t)$ for the case of partial-DTD. Filled triangles connected by the dashed curve denote the survival fraction of the dilated tube $\varphi_o'(t)$ defined for the outer arm for the case of partial DTD. The tube escape time of the outer arm, t^*, is also shown. For further details, see text.

primitive chain having the entanglement segment as the fundamental structural unit. Thus, the test of this picture requires us to know the $\mu(t)$ and $\Phi(t)$ data that are *not* contributed from the local chain motion within the entanglement segment. The viscoelastic relaxation time τ_e of this segment can be evaluated as that of linear PI having $M = M_e$ ($= 5 \times 10^3$); $\tau_e = 2.2 \times 10^{-6}$ s at 40 °C.[16] The corresponding frequency, $1/\tau_e = 4.5 \times 10^5$ s^{-1}, is close to the highest ω examined in Figure 2, indicating that the motion within the entanglement segment contributes to the high ω viscoelastic data shown therein and thus to the spectrum $\{h_p, \tau_{p,G}\}$ at short $\tau_{p,G}$ determined from those data. For this reason, $\mu(t)$ is to be evaluated from a subset of the spectrum $\{h_p, \tau_{p,G}\}$ with $\tau_{p,G}$ above a cutoff time τ_{cut}. Since the upturn of G'' and tan δ attributable to the Rouse motion within the entanglement segment is noted at $\omega > \omega_{upturn} > 2 \times 10^4$ s^{-1} (cf. Figure 2), we chose $\tau_{cut} = 1/\omega_{upturn} = 5 \times 10^{-5}$ s to evaluate $\mu(t)$ as $\mu(t) = \sum_{\tau_{p,G} \geq \tau_{cut}} h_p' \exp(-t/\tau_{p,G})$, where $h_p' = h_p/\{\sum_{\tau_{q,G} \geq \tau_{cut}} h_q\}$ is the normalized intensity of the viscoelastic modes having $\tau_{p,G} > \tau_{cut}$ ($\sum_p h_p' = 1$). This $\mu(t)$ is shown in Figure 4 with the circles. In the range of $t > 10^{-4}$ s where the dominant part of the terminal relaxation of CT-PI is observed, the $\mu(t)$ value was rather insensitive to our choice of τ_{cut}: For an arbitrary choice of τ_{cut}/s between 2×10^{-5} and 1×10^{-4}, $\mu(t)$ at those t changed only by ±15%. Thus, the small uncertainty in the choice of τ_{cut} hardly affects the results of our test of the DTD picture.

The situation is different (better) for the dielectric $\Phi(t)$. PI chains have both type A and type B dipoles parallel and perpendicular to the chain backbone. The dielectric relaxation of PI exclusively detects the fluctuation of the sum of the type A dipoles if the relaxation of the type B dipoles activated by the motion of *monomeric* segments has completed at the frequencies examined. This is the case for the data show in Figure 3; the type B dipole relaxation frequency of PI, $\omega_B = 1.0 \times 10^9$ s^{-1} at 40 °C,[34] is orders of magnitude larger than the highest ω examined in Figure 3. Since the sum of the type A dipoles is proportional to a vector spanning the largest scale of the chain (e.g., end-to-end vector for the case of linear PI chain; this vector for CT-PI is specified later), the chain motion within the entanglement segment (except the segment at the chain end) does not contribute to the dielectric data shown in Figure 3. Thus, we can utilize the whole spectrum determined from those data, $\{g_p, \tau_{p,\varepsilon}\}$ with $\tau_{p,\varepsilon} \geq 3 \times 10^{-6}$ s ($\simeq \tau_e$), to evaluate, with no ambiguity, $\Phi(t) = \sum_p g_p' \exp(-t/\tau_{p,\varepsilon})$ with $g_p' = g_p/\sum_q g_q$ ($\sum_p g_p' = 1$). This $\Phi(t)$ is shown in Figure 5 with circles. (We also examined numerical accuracy of $\Phi(t)$ by re-evaluating it from a subset of the spectrum, $\{g_p, \tau_{p,\varepsilon}\}$ with $\tau_{p,\varepsilon} \geq \tau_{cut}$, as did for the viscoelastic $\mu(t)$. At $t > 10^{-4}$ s where the dominant part of CT-PI relaxation occurs, the $\Phi(t)$ value changed only by 8% on a significant increase of τ_{cut}/s from 3×10^{-6} ($= 1.4\tau_e$) to 1×10^{-4} because the dielectric modes with $\tau_{p,\varepsilon} < 1 \times 10^{-4}$ s had just small intensities g_p. This result confirms the accuracy of $\Phi(t)$ (much better than 8%) shown in Figure 5.

3.2. Terminal Relaxation Time and Mode Distribution of CT-PI. For regularly star-branched chains, a *span* is defined as the longest linear portion of the chain that covers the whole chain, i.e., the portion spanning two free ends of two arms (going through the branching point).[3,35] Similarly, the span for the CT-PI chain is defined as a portion spanning the free ends of two outer arms attached to different inner arms, i.e., the portion having the molecular weight of $M_{span} = 2M_i + 2M_o$ ($= 74.0 \times 10^3$); cf. Figure 1a. Correspondingly, the half-span is defined as the linear portion composed of one of the three inner arms and one of the two outer arms grafted thereto. (The other outer arm bifurcates from this linear half-span portion.)

In Figure 6, the terminal dielectric and viscoelastic relaxation times (second-moment average relaxation times[3]) of CT-PI at 40 °C evaluated from the data in Figures 2 and 3, $\langle\tau_\varepsilon\rangle_w \equiv [\{\varepsilon_0 - \varepsilon'\}/\omega\varepsilon'']_{\omega\to 0}$ and $\langle\tau_G\rangle_w \equiv [G'/\omega G'']_{\omega\to 0}$ are double-logarithmically plotted against M_{span}; see filled square and circle. For comparison, the previously reported $\langle\tau_\varepsilon\rangle_w$ and $\langle\tau_G\rangle_w$ data for star PI[16] at 40 °C are also plotted against M_{span} ($= 2M_{arm}$ for this case); cf. unfilled squares and circles. Clearly, the terminal relaxation of CT-PI is slower, by a factor of ≃10, than the star PI of the same M_{span}. This result demonstrates that the outer arm grafted on the half-span portion of CT-PI retards the global (terminal) relaxation significantly.

In Figures 2 and 3, we note that CT-PI exhibits two-step relaxation qualitatively similar to that observed for Cayley-tree polybutadienes (PB);[29] see the G'' and ε'' data of CT-PI at $\omega < 10^4$ s^{-1}. This fact suggests that CT-PI relaxes hierarchically from the outer arm toward the inner arm. The terminal frequency of the fast relaxation process, ω_{fast}, is useful for examining details of this hierarchical behavior. The ω_{fast} is not so easily evaluated from the G'' and ε'' data because the two-step relaxation of CT-PI is considerably broad. However, we may still obtain a rough estimate as a frequency for the tan δ

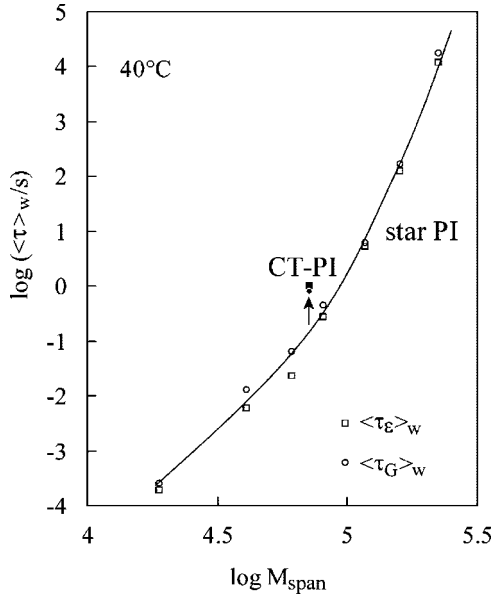

Figure 6. Dielectric and viscoelastic terminal relaxation times, $\langle\tau_\varepsilon\rangle_w$ and $\langle\tau_G\rangle_w$ (filled square and circle), obtained for CT-PI at 40 °C. For comparison, $\langle\tau_\varepsilon\rangle_w$ and $\langle\tau_G\rangle_w$ data for star-branched PI at 40 °C are also shown (unfilled squares and circles).

inflection seen at around the low ω end of the fast process, $\omega_{fast} = 100-200\ s^{-1}$ (see bottom panel of Figure 2). The hierarchical character of CT-PI relaxation can be confirmed from this ω_{fast} as well as the data for the tube survival fraction, as explained later in more detail.

In relation to the two-step relaxation behavior, it is also informative to examine a molecular meaning of the broad G'' peak of CT-PI seen at $\omega/s^{-1} = 10^3-10^4$ (cf. top panel of Figure 2). This peak looks similar to a peak observed for regular star PI[35] and may be assigned as the *intrinsic* (entanglement-free) Rouse fluctuation of the arms of CT-PI. The viscoelastic Rouse fluctuation frequency of the star arm, $\omega_{f,G}$ ($\propto M_{arm}^{-2}$), can be estimated from $\langle\tau_G\rangle_{w,star}$ data of nonentangled PI.[16] The frequency thus estimated for the outer arm of our CT-PI ($M_o = 12.3 \times 10^3$), $\omega_{f,G} = 1.8 \times 10^4\ s^{-1}$, is well above the G'' peak frequency ($\simeq 2 \times 10^3\ s^{-1}$). This fact suggests that the dominant part of the relaxation reflected in the broad G'' peak of our CT-PI is not attributable to the Rouse fluctuation of the outer arm alone. A similar result is noted for previously examined Cayley-tree PB[29] as well as comb-type PB and polystyrene (PS).[20]

For a star arm with $M_{arm} = 37.0 \times 10^3$ being identical to $M_{span}/2$ for CT-PI, $\omega_{f,G}$ is estimated to be $2.0 \times 10^3\ s^{-1}$. The broad G'' peak of CT-PI is observed at around this $\omega_{f,G}$ (cf. arrow in top panel of Figure 2), suggesting that this peak reflects the intrinsic Rouse fluctuation of the half-span of CT-PI. The same assignment can be made for the broad peak of ε'' seen at high ω: The dielectric Rouse fluctuation frequency for the half-span, $\omega_{f,\epsilon} \simeq 1.0 \times 10^3\ s^{-1}$ ($= \omega_{f,G}/2$), is close to the ε'' peak frequency (see the arrow in Figure 3). Thus, the half-span appears to behave as an *effective* arm for CT-PI in the Rouse fluctuation regime. A consequence of this fluctuation in the hierarchical character of CT-PI relaxation is later discussed in relation to the data for the survival fraction of the dilated tube.

Since the half-span includes the outer branching point (bifurcation point between the inner and outer arms), this point should fluctuate at least moderately during the Rouse fluctuation of the half-span as a whole. One may argue that the branching point of the (primitive) chain considered in this paper does not fluctuate at short t where the tube is fixed. However, this fluctuation is activated whenever the constraint release mechanism dilates the tube. Indeed, the DTD analysis explained later suggests that the tube diameter dilates by 15% in a time scale of $t \simeq 10^{-3}$ s, i.e., in a frequency scale of $\omega \simeq 10^3\ s^{-1}$ where the broad G'' and ε'' peaks are observed. This extent of dilation seems to be sufficient to activate the Rouse fluctuation of the half-span as a whole, thereby allowing the half-span to behave as the effective arm.

3.3. Relationship between Dielectric Relaxation Function and Tube Survival Fraction. The test of the full- and partial-DTD pictures (eqs 2 and 3) requires us to evaluate the survival fraction of the dilated tube $\varphi'(t)$ from the data of the normalized dielectric relaxation function, $\Phi(t)$, shown in Figure 5 with circles. For this evaluation, we first need to express $\Phi(t)$ in terms of the end-to-end vectors $\mathbf{R}$ of the arms of the CT-PI chain.

The arms of the CT-PI chains have type A dipoles parallel along their backbone, and the microscopic polarization is given by a sum of these type A dipoles. The dielectric relaxation detects a memory decay (autocorrelation) of this polarization.[3,36] Within the context of the tube model, we choose the entanglement segment (of the size a) as the structural unit of the CT-PI chain and regard the central branching point of this chain to be fixed in space until the global relaxation completes. (The local motion within the entanglement segment has been equilibrated in the time scale considered in our analysis.) Then, the memory is to be evaluated for a group of three arms, an inner arm and two outer arms grafted thereto. This group is schematically shown in Figure 1b.

Both of the outer and inner arms of our CT-PI chain have type A dipoles converging toward the central branching point, as explained earlier. Thus, the microscopic polarization $\mathbf{P}$ of the group of the arms (= sum of the type A dipoles in this group) is proportional to a vectorial sum $-\{\mathbf{R}_i + \mathbf{R}_{o1} + \mathbf{R}_{o2}\}$, where $\mathbf{R}_i$ (shown in Figure 1b) is the vector connecting the central branching point to the outer branching point and $\mathbf{R}_{ok}$ (not shown) is the vector connecting the outer branching point to the free end of kth outer arm ($k = 1$ and 2). (These $\mathbf{R}$'s are the end-to-end vectors of respective arms.)

Considering the above feature of $\mathbf{P}$, we can express $\Phi(t)$ as the autocorrelation of $\mathbf{R}$'s at two separate times, t and 0:

$$\Phi(t) = \frac{\langle \mathbf{P}(t)\cdot\mathbf{P}(0)\rangle}{\langle\{\mathbf{P}(0)\}^2\rangle} = \frac{\langle\{\mathbf{R}_i(t) + \mathbf{R}_{o1}(t) + \mathbf{R}_{o2}(t)\}\cdot\{\mathbf{R}_i(0) + \mathbf{R}_{o1}(0) + \mathbf{R}_{o2}(0)\}\rangle}{\langle\{\mathbf{R}_i(0) + \mathbf{R}_{o1}(0) + \mathbf{R}_{o2}(0)\}^2\rangle} \quad (5)$$

Here, $\langle\cdots\rangle$ indicates an ensemble average taken for all chains in the system. Since the inner and outer arms have the Gaussian conformation, they have no isochronal orientational correlation in their end-to-end vectors. Thus, eq 5 is rewritten as

$$\Phi(t) = \frac{\langle\{\mathbf{R}_i(t) + \mathbf{R}_{o1}(t) + \mathbf{R}_{o2}(t)\}\cdot\{\mathbf{R}_i(0) + \mathbf{R}_{o1}(0) + \mathbf{R}_{o2}(0)\}\rangle}{(N_i + 2N_o)a^2} \quad (6)$$

N_i and N_o are the number of entanglement segments per inner and outer arm, respectively, and a is the size of this segment: The N_i value is very close to the $2N_o$ value for our CT-PI having $M_i = 24.7 \times 10^3$ and $M_o = 12.3 \times 10^3$.

We can express the averages appearing in eq 6, $\langle\mathbf{R}_\alpha(t)\cdot\mathbf{R}_\beta(0)\rangle$ with α, β = i, o1, o2, in terms of $\mathbf{R}_\alpha(0)$, $\mathbf{R}_\beta(0)$, and the displacements $\mathbf{D}_{\alpha'}$ (α' = i, o1, o2; cf. Figure 1b) to formulate the relationship between $\Phi(t)$ and the tube survival fraction $\varphi'(t)$, as explained in Appendix A in detail. A brief summary of this formulation is given below, first for the early stage of relaxation where the outer arm has not fully relaxed and then for the late stage where this full relaxation has occurred. (Since $\varphi'(t)$ is not

largely different from $\Phi(t)$ in a numerical sense, readers not interested in details of the formulation may skip the following subsections and directly proceed to section 3.4.)

3.3.1. $\Phi(t)-\varphi'(t)$ Relationship in Early Stage. In Figure 1b, the thick dashed curve illustrates the conformation of the group of inner and outer arms at time 0. The thick solid curve shows the conformation at time t (>0) in an early stage of relaxation where a fraction $\varphi_o'(t)$ of the entanglement segments of the outer arm has not relaxed. The surviving part of the tube that constrains these segments dilates to a diameter $a'(t)$, and the whole segments of the inner arm remain in this dilated tube. $a'(t)$ is considered to be the same for the portions of the tube constraining the outer and inner arms. In this situation, the tube survival fraction averaged for the inner and outer arms is written as

$$\varphi'(t) = \frac{N_i + 2N_o\phi_o'(t)}{N_i + 2N_o} \quad \text{(early stage of relaxation)} \qquad (7)$$

A relationship between $\varphi_o'(t)$ and $\varphi'(t)$ equivalent to eq 7, $\varphi_o'(t) = \{(N_i + 2N_o)/2N_o\}\varphi'(t) - N_i/2N_o$ ($= 2\varphi'(t) - 1$ for our CT-PI), is later utilized to evaluate $\varphi_o'(t)$ from $\varphi'(t)$ data and examine the hierarchical character of CT-PI relaxation.

Now, we consider a change of the chain conformation in the interval of time between 0 and t (cf. Figure 1b). In this interval, the outer branching point and the entanglement segment on the dilated tube edge (tube-edge segment) exhibit respective displacements, $\mathbf{D}_i$ and $\mathbf{D}_{ok}$ ($k = 1, 2$); cf. Figure 1b. The $\langle \mathbf{R}_\alpha(t)\cdot\mathbf{R}_\beta(0)\rangle$ terms (α, β = i, o1, o2) appearing in eq 6 are contributed from cross-correlation of $\mathbf{R}_\beta(0)$ with the displacements $\mathbf{D}$: For example, the $\langle \mathbf{R}_i(t)\cdot\mathbf{R}_i(0)\rangle$ term is given by a sum of $\langle\{\mathbf{R}_i(0)\}^2\rangle$ ($= N_i a^2$; mean-square end-to-end distance of inner arm) and the cross-correlation, $\langle \mathbf{R}_i(0)\cdot\mathbf{D}_i\rangle$. These cross-correlation terms are analyzed in Appendix A to derive the relationship between $\Phi(t)$ and $\varphi'(t)$. The result is summarized as

$$\Phi(t) = \varphi'(t) - \frac{3}{8(N_i+2N_o)}\left\{\frac{a'(t)}{a} - 1\right\}^2\left\{1 - \frac{4}{3}Q_{oi}(t) + \frac{2}{3}Q_{oo}(t)\right\} \quad \text{for } N_o > \beta(t) \text{ and } \varphi'(t) > v_i \ (t < t^*) \qquad (8)$$

Here, the term $\{a'(t)/a - 1\}^2$ represents the mean-square displacement $\langle \mathbf{D}^2\rangle$ of the tube-edge segment/branching point reduced by a factor of $a^2/4$; $\langle \mathbf{D}^2\rangle = \langle \mathbf{D}_i^2\rangle = \langle \mathbf{D}_{ok}^2\rangle$ (cf. Appendix A). This $\langle \mathbf{D}^2\rangle$ was evaluated as the mean-square distance between centers of two entanglement segments of size a randomly located on the cross section/edge of the dilated tube of the diameter $a'(t)$.[10,37] The functions $Q_{oo}(t) \equiv \langle \mathbf{D}_{o1}\cdot\mathbf{D}_{o2}\rangle/\langle \mathbf{D}^2\rangle$ and $Q_{oi}(t) \equiv \langle \mathbf{D}_{ok}\cdot\mathbf{D}_i\rangle/\langle \mathbf{D}^2\rangle$ ($k = 1, 2$) represent growth of the cross-correlation of the displacements $\langle \mathbf{D}_{o1}\cdot\mathbf{D}_{o2}\rangle$ and $\langle \mathbf{D}_{ok}\cdot\mathbf{D}_i\rangle$ with time relative to the growth of $\langle \mathbf{D}^2\rangle$. The functional forms of $Q_{oo}(t)$ and $Q_{oi}(t)$ for the Rouse-CR mechanism are shown in Appendix B.

Note that eq 8 is valid only when (1) N_o is larger than the number $\beta(t)$ of entanglement segments per dilated segment so that the outer arm is composed of more than one dilated segment and (2) $\varphi'(t)$ is larger than the volume fraction v_i of the inner arm so that the outer arm has not fully escaped from the dilated tube; i.e., t is shorter than the *tube escape time of the outer arm*, t^*. Condition (2) in turn enables us to evaluate t^* from the $\varphi'(t)$ data through a relationship, $\varphi'(t^*) = v_i$. The hierarchical character of CT-PI relaxation is examined later on the basis of the t^* value.

In relation to this condition (2), a comment needs to be added for the functions $Q_{oo}(t)$ and $Q_{oi}(t)$ defined above. The tube-edge segment coincides with the segment at the outer branching point when the outer arm has just escaped from the dilated tube at t^* (cf. Figure 1b); namely, $\langle \mathbf{D}_{o1}\cdot\mathbf{D}_{o2}\rangle = \langle \mathbf{D}_{ok}\cdot\mathbf{D}_i\rangle = \langle \mathbf{D}^2\rangle$ at t^*. Thus, $Q_{oo}(t)$ and $Q_{oi}(t)$ (≥ 0) increase to unity with increasing t to t^*. In addition, $Q_{oi}(t) \geq Q_{oo}(t)$ at $t < t^*$ because the contour distance between the outer branching point and the tube-edge segment is smaller than the distance between two different tube-edge segments (cf. Figure 1b). These general features of Q's, rather than their detailed functional forms, play a key role in the dielectric evaluation of $\varphi'(t)$, as explained later in more detail.

3.3.2. $\Phi(t)-\varphi'(t)$ Relationship in Late Stage. In the late stage of relaxation where $N_o < \beta(t)$ and/or $\varphi'(t) < v_i$ ($t > t^*$), only a fraction of the inner arm segments is constrained in the surviving portion of the dilated tube. For this case, $\Phi(t)$ is not contributed from the cross-correlation of the displacements $\mathbf{D}_i$ and $\mathbf{D}_{ok}$ ($k = 1, 2$), and the relationship between $\varphi'(t)$ and $\Phi(t)$ can be easily formulated as (see Appendix A)

$$\Phi(t) = \varphi'(t) - \frac{1}{8(N_i+2N_o)}\left\{\frac{a'(t)}{a} - 1\right\}^2 \quad \text{for } \beta(t) < N_i + 2N_o \text{ and } 1/(N_i+2N_o) < \varphi'(t) < v_i \qquad (9)$$

This equation loses its sound meaning when the inner arm and two outer arms attached thereto are equilibrated as a whole ($\beta(t) > N_i + 2N_o$) and/or less than one entanglement segment remains in the dilated tube ($(N_i + 2N_o)\varphi'(t) < 1$). Note that eqs 8 and 9 give the same $\varphi'(t)$ value at the tube escape time of the outer arm, t^* (cf. $Q_{oi}(t^*) = Q_{oo}(t^*) = 1$ in eq 8).

Since $a'(t)$ is expressed in terms of $\varphi'(t)$ and/or the CR-equilibration number $\beta_{CR}(t)$ as shown in eqs 2 and 3, $\varphi'(t)$ can be experimentally evaluated from the $\Phi(t)$ data (plus CR time data giving $\beta_{CR}(t)$) with the aid of eqs 8 and 9. We make this evaluation to test the DTD picture in the following sections.

3.4. Test of Full-DTD Picture. In the full-DTD picture, the $a'(t)/a$ ratio is expressed only in terms of the tube survival fraction $\varphi'(t)$: $a'(t)/a = \{\varphi'(t)\}^{-d/2}$ (eq 2). The dilation exponent for PI, $d = 1.3$, has been determined experimentally (without utilizing any specific molecular model) from viscoelastic data of binary blends of linear PI having widely separated molecular weights.[11] (The blends exhibited two-step rubbery plateau when the volume fraction v_2 of high-M component chains therein was large and these chains were mutually entangled. The low-ω plateau height was found to scale as $v_2^{2.3}$, not as $v_2^{2.0}$, thereby giving $d = 1.3$.[11] The value of the dilation exponent will be further discussed in our future paper.[38])

Thus, for a given set of N_i and N_o (and the cross-correlation functions $Q_{oi}(t)$ and $Q_{oo}(t)$), eqs 8 and 9 become closed equations that enable us to evaluate $\varphi'(t)$ from the $\Phi(t)$ data shown in Figure 5. Our CT-PI sample has $M_i/M_e = 4.9_4$ and $M_o/M_e = 2.4_6$ ($M_e = 5 \times 10^3$ PI[33,39]). Despite those noninteger values of M/M_e, the number of entanglement segments per inner and outer arms, N_i and N_o, are to be chosen as integers within the context of the Rouse-CR analysis (Appendix B) required for the test of the DTD picture. Furthermore, the fact that the M_i/M_o ratio ($= N_i/N_o$) is very close to an integer value of 2 plays an important role in this analysis. For these reasons and for definiteness, we choose $N_i = 6$ and $N_o = 3$ to evaluate $\varphi'(t)$ and test the validity of eq 2. We confirmed that the results described in this and next sections do not change significantly even for the other choice of $N_i = 2N_o = 4$. (The choice of $N_i = 6$ and $N_o = 3$ coincidentally corresponds to a choice of $M_e = 4 \times 10^3$, a M_e value being close to that adopted by van Ruymbeke et al.[29])

The $\varphi'(t)$ thus obtained for $N_i = 2N_o = 6$ is plotted against t in Figure 5 (asterisk), and the corresponding number of entanglement segments per dilated segment, $\beta_{f\text{-}DTD}(t) = \{\varphi'(t)\}^{-d}$ ($d = 1.3$), is plotted in Figure 7 (circles). These plots were made in the following way.

Since the chain displacement on tube edge unavoidably leads to the dielectric relaxation but not necessarily decreases $\varphi'(t)$, we note an obvious feature that $\Phi(t) \leq \varphi'(t)$. Furthermore, the cross-correlation functions $Q_{oi}(t)$ and $Q_{oo}(t)$ included in eq 8

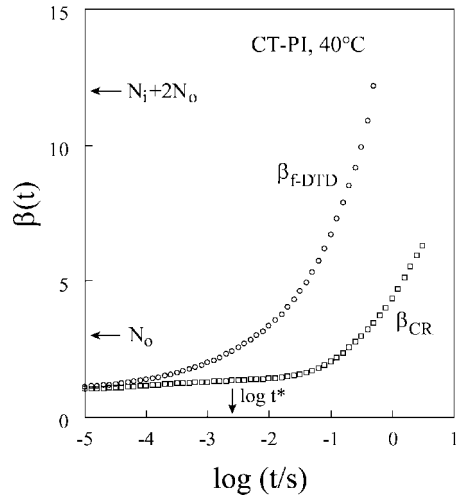

Figure 7. Number of entanglement segments $\beta(t)$ of CT-PI that are mutually equilibrated to be coarse-grained into a dilated segment in time scale, t. The circles indicate the number deduced for the case of full DTD, $\beta_{f\text{-}DTD}(t) = \{\varphi'(t)\}^{-d}$ with $d = 1.3$. Squares show the maximum possible number allowed by Rouse-CR mechanism, $\beta_{CR}(t)$. The tube escape time of the outer arm, t^*, is also shown. For further details, see text.

satisfy a relationship $Q_{oi}(t) \geq Q_{oo}(t)$, and both $Q_{oi}(t)$ and $Q_{oo}(t)$ increase to unity with increasing t to the tube escape time of the outer arm, t^*. We considered these general features to make trial choices, $Q_{oi}(t) = Q_{oo}(t) = 0$ and $Q_{oo}(t) = 2Q_{oi}(t) - 3/2$ ($\leq Q_{oi}(t)$), giving the upper and lower bound values of $\varphi'(t)$, respectively. (The latter choice gives $\varphi'(t) = \Phi(t)$; cf. eq 8.) These trial choices were made to just specify the range of t where eq 8 was valid. For respective choices, we calculated $\varphi'(t)$ and $\beta_{f\text{-}DTD}(t)$ from the $\Phi(t)$ data by utilizing eq 8 with $a'(t)/a$ being replaced by $\{\varphi'(t)\}^{-d/2}$ ($d = 1.3$). Actually, the upper and lower bound values of $\varphi'(t)$ differed by less than 4% in a range of $t < 7 \times 10^{-3}$ s because the term in eq 8 including $Q_{oi}(t)$ and $Q_{oo}(t)$ was just a minor correction term at those t. For both choices, we found two critical times in this range of t, a time t_β ($= 6.3 \times 10^{-3}$ s) where $\beta_{f\text{-}DTD}(t)$ increased to N_o, and the tube escape time of the outer arm t^* ($= 2.5 \times 10^{-3}$ s) where $\varphi'(t)$ decreased to v_i ($= 0.5$); cf. Figures 5 and 7. Following the validity criteria for eq 8, $N_o > \beta(t)$ and $\varphi'(t) > v_i$, we limited the use of eq 8 only at $t < t^*$ (where the two choices gave the $\varphi'(t)$ values differing by less than 2%).

The first choice giving the upper bound of $\varphi'(t)$ violates the requirement of continuity with eq 9 ($Q_{oi}(t^*) = Q_{oo}(t^*) = 1$) while the second choice giving the lower bound does not account for the dielectric relaxation activated by the displacement at the dilated tube edge. Because of this inconsistency, *neither* of the two choices can be adopted in the *analytical* sense, although these choices allowed us to determine t^* ($= 2.5 \times 10^{-3}$ s) with negligible ambiguity. Thus, $Q_{oi}(t)$ and $Q_{oo}(t)$ being derived from the Rouse-CR analysis and satisfying this analytical consistency (cf. Appendix B) were utilized in eq 8 as the final choice to calculate $\varphi'(t)$ at $t < t^*$. (The cross-correlation represented by these Q's grew significantly only when t was increased above $0.6t^*$ and the edges of the surviving portion of the dilated tube came into the close vicinity of the outer branching point; cf. Appendix B.) Since the upper and lower bound values of $\varphi'(t)$ agreed within 2% at those t, the final $\varphi'(t)$ data thus obtained were also in this range of agreement. (Actually, any functional form of $Q(t)$ exhibiting the general features explained earlier, e.g., $Q(t) = (t/t^*)^p$ with $p > 0$, gave the $\varphi'(t)$ value that agreed with the final $\varphi'(t)$ data within 2%.)

At $t > t^*$, we utilized eq 9 to evaluate $\varphi'(t)$ and $\beta_{f\text{-}DTD}(t)$. (Equations 8 and 9 gave the same $\varphi'(t^*)$ and $\beta_{f\text{-}DTD}(t^*)$ values.) The resulting $\beta_{f\text{-}DTD}(t)$ increased to $N_i + 2N_o$ ($= 12$) at $t = 0.5$ s where $\varphi'(t)$ had not yet decreased to $1/(N_i + 2N_o)$. Because of the validity criteria for eq 9, $\beta(t) < N_i + 2N_o$ and $1/(N_i + 2N_o) < \varphi'(t)$, we evaluated $\varphi'(t)$ and $\beta_{f\text{-}DTD}(t)$ only up to $t = 0.5$ s.[40]

In Figure 5, the asterisk indicates the $\varphi'(t)$ data obtained as above in the entire range of $t \leq 0.5$ s. These $\varphi'(t)$ data were well described by an empirical equation written as a sum of exponential decay terms, as indicated with the dotted curve. We utilized this empirical equation to evaluate the normalized viscoelastic relaxation function for the case of full-DTD, $\mu_{f\text{-}DTD}(t) = \{\varphi'(t)\}^{1+d}$ with $d = 1.3$ for PI. The results are shown in Figure 4 with the dotted curve. $\mu_{f\text{-}DTD}(t)$ is significantly smaller than the $\mu(t)$ data (circles) at $t > 10^{-3}$ s, even in a range of $10^{-3} < t/s < 10^{-1}$ where $\varphi'(t)$ is almost indistinguishable from the $\Phi(t)$ data (cf. Figure 5). This difference between $\mu_{f\text{-}DTD}(t)$ and the $\mu(t)$ data is well beyond the experimental uncertainty. (From the uncertainties in the $\mu(t)$, $\Phi(t)$, and $\varphi'(t)$ data explained earlier, the total uncertainty in the comparison in Figure 4 is estimated to be less than 30%.) Thus, we can unequivocally conclude that the full-DTD picture fails for the dominant part of the terminal relaxation of our CT-PI. This result is in harmony with the result obtained for star PI.[10,16–18]

3.5. Evaluation of Number of CR-Equilibrated Entanglement Segments. The test of the partial-DTD picture requires us to evaluate the maximum possible number $\beta_{CR}(t)$ of the entanglement segments that can be mutually equilibrated through the CR mechanism in the given time scale t (cf. eq 3). This $\beta_{CR}(t)$ is defined as a reciprocal of a normalized relaxation function $\psi_{CR}(t)$ that represents a *hypothetical* stress decay *due only to* CR.[10,41] This decay is well described by the Rouse-type dynamics having the dielectric CR time $2\tau_G^{CR}$ as the longest relaxation time, as found star PI and blends of linear PI.[9,10,41] Specifically, for the star PI, $\psi_{CR}(t)$ is written in the Rouse form for a tethered linear chain.[10,41] Correspondingly, we may formulate $\psi_{CR}(t)$ for our CT-PI as the Rouse function for a tethered and bifurcated chain composed of three arms, a tethered inner arm having N_i (=6) segments and two outer arms each having N_o (=3) segments (cf. Figure 1b). Strictly speaking, the actual CR dynamics of CT-PI may have a distribution of the local CR hopping time and deviate from the Rouse-CR dynamics without this distribution. However, following the strategy of this paper (minimization of the reliance on delicate/detailed model assumptions), we here utilize the simplest Rouse-CR dynamics to formulate $\psi_{CR}(t)$.

The explicit functional form of this $\psi_{CR}(t)$ can be obtained from the Rouse eigenmode analysis; see Appendix B. The result is summarized as

$$\psi_{CR}(t) = \frac{1}{4N_o}\left[\sum_{p=1}^{4N_o-N_f} \exp\left(-\frac{r_p t}{2\tau_G^{CR}}\right) + \sum_{q=1}^{N_f} \exp\left(-\frac{(2q-1)^2 t}{\tau_f}\right)\right] \tag{10}$$

with

$$\text{for } p = 4k+1 \text{ (=multiple of 4 plus 1):} \quad r_p = \left\{1 + \frac{k\pi}{\theta}\right\}^2 \quad (k = 0, 1, 2, \ldots) \tag{11a}$$

$$\text{for } p = 4k+2 \text{ and } 4k+3 \text{ (= multiple of 4 plus 2 and/or 3):} \quad r_p = \left\{\frac{(k+1/2)\pi}{\theta}\right\}^2 \quad (k = 0, 1, 2, \ldots) \tag{11b}$$

$$\text{for } p = 4k+4 \text{ (= multiple of 4):} \quad r_p = \left\{-1 + \frac{(k+1)\pi}{\theta}\right\}^2 \quad (k = 0, 1, 2, \ldots) \tag{11c}$$

and

$$\theta = \sin^{-1}\left(\frac{1}{\sqrt{6}}\right) \quad (= 0.13386\pi) \tag{11d}$$

The first summation in the square bracket of eq 10 represents the stress decay due to Rouse-CR eigenmodes: Details of the decay rate coefficients r_p (eqs 11a–11c) are explained later. The second summation in eq 10 denotes the stress decay due to a fast CR process activated by the shallow arm retraction (not affected by the retraction potential). This shallow retraction is equivalent to the intrinsic (entanglement-free) Rouse fluctuation of the arms[10,41] having the longest fluctuation time τ_f and the total mode number N_f. This intrinsic Rouse contribution, corresponding to the G'' and ε'' peaks seen at $\omega/s^{-1} = 10^3-10^4$ in Figures 2 and 3, cannot be neglected for star PI at short t[10,41] and thus has been included in eq 10 for CT-PI as a *minor correction* at short t. In eq 10, this contribution has been approximated as that for the tethered linear chain for simplicity.

As explained earlier for Figure 3, the ε'' peak of our CT-PI is attributable to the intrinsic Rouse fluctuation of its half-span (having the molecular weight $M_i + M_o$) rather than the fluctuation of the outer arm alone. Thus, τ_f appearing in eq 10 can be estimated as $1/\omega_{f,\varepsilon} = 1.0 \times 10^{-3}$ s, with $\omega_{f,\varepsilon}$ being the dielectric Rouse fluctuation frequency for the half-span explained earlier (cf. arrow in Figure 3). For the arm of the star PI being composed of N entanglement segments and exhibiting N CR modes, a fraction of the CR modes occurring through the Rouse fluctuation is estimated to be $N^{-1/2}$ and thus $N_f \simeq N^{1/2}$, as discussed previously.[10,41] For our CT-PI chain, N_f can be similarly estimated from the number of the entanglement segments in the half-span, $N_i + N_o$ (= 9), as $N_f = (N_i + N_o)^{1/2} = 3$. (Since the two outer arms are equivalently involved in the half-span, N_f for CT-PI might be somewhat larger than $(N_i + N_o)^{1/2}$. However, for definiteness, we chose $N_f = (N_i + N_o)^{1/2}$ in this paper.)

For the tethered/bifurcated chain with $N_i = 2N_o$, the Rouse-CR eigenmodes are split into four series, as shown in Appendix B. The decay rate coefficient r_p (p = 1, 2, 3,...) specified by eqs 11a–11c is a ratio of the relaxation time of the slowest dielectric CR mode ($=2\tau_G^{CR}$) to that of kth mode in each series (k = 0, 1, 2,...); see eqs 11a–11c for the relationship between p and k. The mode splitting behavior is sensitively affected by the N_i/N_o ratio, and our CT-PI with $N_i/N_o = 2$ has dually degenerated eigenmodes indexed with the mode number $p = 4k + 2$ and $4k + 3$; cf. eq 11b. (Because of this sensitivity, the M_i/M_o ratio being very close to 2 was faithfully transferred to the integer N_i/N_o ratio of 2 in our analysis.)

In general, the viscoelastic CR time τ_G^{CR} (appearing in eq 10) can be determined from the viscoelastic data for binary blends, as reported for blends of linear[42] and/or star PI.[10] However, no such blend data are available for CT-PI chains. Thus, we estimated τ_G^{CR} of our CT-PI from the τ_G^{CR} data available for a series of monodisperse star PI,[10,41] as described in Appendix C. The estimate, $\tau_G^{CR} \simeq 7.3$ s for our CT-PI, as well as τ_f ($= 1.0 \times 10^{-3}$ s) and N_f (=3) evaluated earlier were utilized in eq 10 to calculate the hypothetical CR stress-decay function $\psi_{CR}(t)$. The first summation in the square bracket in eq 10 was taken for the slowest nine Rouse-CR eigenmodes (cf. $4N_o - N_f = 9$). The maximum possible CR-equilibration number of the entanglement segments, $\beta_{CR}(t) = 1/\psi_{CR}(t)$, is shown with the squares in Figure 7. This $\beta_{CR}(t)$ is smaller than $\beta_{f\text{-}DTD}(t)$ for full-DTD (circles), in particular at $t > 10^{-3}$ s where the dominant part of the terminal relaxation of CT-PI is observed. Thus, the large-scale equilibration over $\beta_{f\text{-}DTD}(t)$ segments assumed in the full-DTD picture is not allowed by the Rouse-CR mechanism, which naturally results in the failure of this picture explained earlier. We also note that $\beta_{CR}(t)$ increases to 1.3 at $t \simeq 10^{-3}$ s, and thus the tube has been already dilated to some extent at this short t. This increase, corresponding to 15% dilation of $a'(t)$, appears to allow the intrinsic Rouse fluctuation (shallow retraction) of the effective arm of CT-PI (= half-span having $M_{span}/2 = 37.0 \times 10^3$) explained earlier.

3.6. Test of Partial-DTD Picture. From the results seen in Figure 7 ($\beta_{CR}(t) \leq \beta_{f\text{-}DTD}(t)$ in the entire range of t), the normalized viscoelastic relaxation function for this picture, $\mu_{p\text{-}DTD}(t)$ (eq 3), is given by $\varphi'(t)/\beta_{CR}(t)$. The corresponding tube survival fraction $\varphi'(t)$ was evaluated from eqs 8 and 9 with $a'(t)/a = \{\beta_{CR}(t)\}^{1/2}$. We made this evaluation according to the validity criteria for eqs 8 and 9, as did for the case of full-DTD. First, we made trial choices giving the upper and lower bound values of $\varphi'(t)$, $Q_{oi}(t) = Q_{oo}(t) = 0$ and $Q_{oo}(t) = 2Q_{oi}(t) - 3/2$, to specify the range of t where eq 8 was valid. For both choices, $\varphi'(t)$ decreased to v_i (=0.5) with increasing t up to $t^* = 2.5 \times 10^{-3}$ s (= tube escape time of the outer arm), while $\beta_{CR}(t)$ remained smaller than N_o at $t \leq t^*$. Thus, eq 8 was valid at $t < t^*$, and the difference of the upper and lower bound values of $\varphi'(t)$ at those t was less than 0.2%. Because of the analytical inconsistency in those choices explained earlier, the final $\varphi'(t)$ data at $t < t^*$ were evaluated by utilizing $Q_{oi}(t)$ and $Q_{oo}(t)$ derived from the Rouse-CR analysis in Appendix B. (Actually, any functional form of $Q(t)$ exhibiting the general features explained earlier gave the $\varphi'(t)$ value that agreed with the final $\varphi'(t)$ data within 0.2%.) At $t > t^*$, $\varphi'(t)$ ($< v_i$) was evaluated with eq 9 until it decreased to $1/(N_i + 2N_o)$ at $t = 0.63$ s ($\beta_{CR}(t)$ remained smaller than $N_i + 2N_o$ at those t).

In Figure 5, the $\varphi'(t)$ data thus obtained in the whole range of $t \leq 0.63$ s are shown with small squares.[40] These $\varphi'(t)$ data were well described by an empirical equation written as a sum of exponential decay terms, as shown with the solid curve. The filled triangles connected by the dashed curve indicate the tube survival fraction for the outer arm $\varphi_o'(t)$ evaluated from the $\varphi'(t)$ data with the aid of the relationship equivalent to eq 7, $\varphi_o'(t) = \{(N_i + 2N_o)/2N_o\}\varphi'(t) - N_i/2N_o$ ($= 2\varphi'(t) - 1$ for our CT-PI). This $\varphi_o'(t)$ and the tube escape time of the outer arm, t^* ($= 2.5 \times 10^{-3}$ s), are later utilized to examine the hierarchical character of CT-PI relaxation.

Now, we test the partial-DTD picture. For this purpose, $\mu_{p\text{-}DTD}(t)$ was evaluated from the empirical equation for $\varphi'(t)$ explained above and the $\beta_{CR}(t)$ data (Figure 7). The result is shown in Figure 4 with the solid curve. This $\mu_{p\text{-}DTD}(t)$ is close to the $\mu(t)$ data (circles), confirming that the partial-DTD picture successfully describes the relaxation behavior of CT-PI. This success, noted also for star PI,[10,41] is due to the consistent coarse-graining of the length and time scales in the partial-DTD picture achieved on the basis of the Rouse-CR mechanism.

However, we should also note a non-negligible difference between $\mu_{p\text{-}DTD}(t)$ and $\mu(t)$ data. This difference is attributable, at least partly, to a fact that the actual CR mechanism is close but not identical to the Rouse mechanism. For example, this deviation from the Rouse-CR mechanism has been noted for eigenfunctions experimentally determined for linear PI having dipole inversion.[43,44] In addition, the onset of the CR relaxation of a chain (probe) is determined by the relaxation of surrounding chains (i.e., the local CR hopping of the probe begins to occur only after the surrounding chains exhibit considerable relaxation), but this fact is not well incorporated in the Rouse-CR mechanism.[10] Furthermore, the distribution of the local CR hopping time, not considered in the Rouse-CR mechanism, may affect the actual CR mode distribution to some extent. Refinement of the partial-DTD picture through incorporation of these non-Rouse CR features is an interesting/important subject of future work.

3.7. Comments for Hierarchical Relaxation and CR/Partial-DTD of CT-PI. The outer arm of CT-PI escapes from the dilated tube and fully relaxes when the tube survival fraction $\varphi'(t)$ decreases to the inner arm volume fraction v_i (= 0.5), as

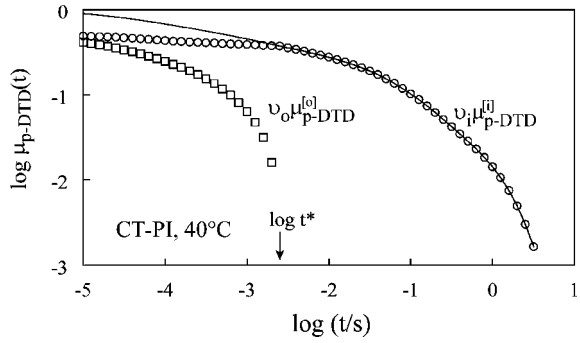

Figure 8. Contributions of the arms to viscoelastic relaxation of the CT-PI chain. $\upsilon_i\mu^{[i]}_{p\text{-}DTD}(t)$ and $\upsilon_o\mu^{[o]}_{p\text{-}DTD}(t)$ for the inner and outer arms are shown with the circle and square, respectively. Solid curve denotes $\mu_{p\text{-}DTD}(t)$ for the CT-PI chain as a whole.

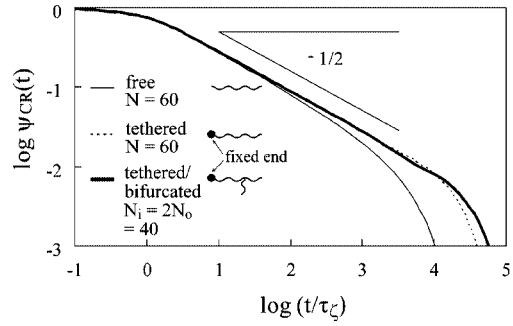

Figure 9. Hypothetical stress decay function due only to Rouse-type CR, $\psi_{CR}(t)$, calculated for free linear, tethered linear, and tethered/bifurcated chains. The free and tethered linear chains have the same segment number ($N = 60$). The tethered/bifurcated chain has the half-span identical to that for the tethered linear chain; $N_i + N_o = N = 60$ ($N_i = 40$, $N_o = 20$) for the former. The calculated $\psi_{CR}(t)$ is plotted against a reduced time, t/τ_ζ, where τ_ζ ($= \zeta_{CR}/2\kappa\pi^2$) represents the local CR hopping time. For further details, see text.

clearly noted from the schematic illustration in Figure 1b. The tube escape time of the outer arm, $t^* = 2.5 \times 10^{-3}$ s, and the tube survival fraction defined for this arm, $\varphi_o'(t)$ (filled triangles in Figure 5), have been experimentally obtained through the test of the partial-DTD picture. These t^* and $\varphi_o'(t)$ data allow us to examine the hierarchical character of CT-PI relaxation, as explained below. (Indistinguishable t^* and $\varphi_o'(t)$ values were also obtained through the test of the full-DTD picture, although this picture was not valid for CT-PI.)

At t^*, the outer arm has not been coarse-grained into one dilated segment ($\beta_{CR}(t^*) \simeq 1.4 < N_o$; cf. Figure 7) but has escaped from the dilated tube to fully relax. The corresponding frequency, $\omega^* = 1/t^* = 400\ s^{-1}$, is fairly close to the terminal frequency of the fast relaxation process estimated earlier in Figure 2, $\omega_{fast} = 100-200\ s^{-1}$. Thus, the dominant part of the relaxation of the CT-PI chain, occurring at $\omega < \omega_{fast} \simeq \omega^*$ (i.e., after the full relaxation of the outer arm), is unequivocally attributed to the relaxation of the inner arm, which lends support to the molecular picture of hierarchical relaxation, the relaxation proceeding from the outer arm to the inner arm.

The $\varphi_o'(t)$ data enable us to examine further details of this hierarchical relaxation. The normalized viscoelastic relaxation function for the case of partial-DTD, $\mu_{p\text{-}DTD}(t) = \varphi'(t)/\beta_{CR}(t)$, agrees satisfactorily with the $\mu(t)$ data (cf. Figure 4). This $\mu_{p\text{-}DTD}(t)$ can be decomposed into the contributions from the inner and (two) outer arms as (cf. eq 7)

$$\mu_{p-DTD}(t) = \upsilon_i\mu^{[i]}_{p-DTD}(t) + \upsilon_o\mu^{[o]}_{p-DTD}(t) \quad \text{with } \mu^{[\alpha]}_{p-DTD} = \frac{\varphi_\alpha'(t)}{\beta_{CR}(t)}\ (\alpha = i, o) \quad (12)$$

Here, $\upsilon_\alpha$and $\mu^{[\alpha]}_{p\text{-}DTD}(t)$ (α = i, o) are the volume fraction and normalized viscoelastic relaxation function defined for respective arms. We evaluated the tube survival fractions defined for the inner arm, $\varphi_i'(t) = \{\varphi'(t) - \upsilon_o\varphi_o'(t)\}/\upsilon_i$, from the $\varphi'(t)$ and $\varphi_o'(t)$ data for the case of partial-DTD (unfilled squares and filled triangles in Figure 5) and further obtained $\mu^{[i]}_{p\text{-}DTD}(t)$ and $\mu^{[o]}_{p\text{-}DTD}(t)$ (eq 12) with the aid of the $\beta_{CR}(t)$ data (Figure 7).

In Figure 8, the viscoelastic contributions of the inner and outer arms thus obtained, $\upsilon_i\mu^{[i]}_{p\text{-}DTD}(t)$ and $\upsilon_o\mu^{[o]}_{p\text{-}DTD}(t)$, are shown with the circle and square, respectively. The solid curve indicates their sum ($= \mu_{p\text{-}DTD}(t)$). The inner arm hardly relaxes until the relaxation of the outer arm completes at $t = t^*$ because $\beta_{CR}(t)$ increases only a little and $\varphi_i'(t)$ remains unity at $t < t^*$, which confirms the hierarchical character of the CT-PI relaxation. Furthermore, the lack of significant viscoelastic relaxation of the inner arm at $t < t^*$ allows us to attribute the fast relaxation process seen in Figure 2 (almost) exclusively to the outer arms. This fast process involves the intrinsic Rouse-like fluctuation of the *half-span* of the CT-PI chain (not just the outer arm) occurring at $\omega_{f,G} \simeq 2.0 \times 10^{-3}\ s^{-1}$, as explained for Figure 2. In other words, the fast process involves the motion of both of the outer and inner arms. Nevertheless, the inner arm hardly relaxes during the fast process because the tube dilates ($\beta_{CR}(t)$ increases) just a little at $t < t^*$, and this arm stays in the dilated tube at those t. It is the $\varphi'(t)$ and t^* data that allowed us to obtain this detailed molecular view, which in turn indicates the importance of the dielectric experiment giving those data.

In relation to the above conclusion, we note that the hierarchical relaxation is a direct consequence of the molecular picture of DTD illustrated in Figure 1b (the inner arm cannot escape from the dilated tube until the outer arms complete the escape). However, we should also note that the full-DTD picture leads to a scenario being different quantitatively from that explained above for the partial-DTD picture. Since $\beta_{f\text{-}DTD}(t)$ for the full-DTD picture considerably increases in the range of $t < t^*$ (cf. Figure 7), this picture suggests that the inner arm relaxes considerably during the fast process ($\mu^{[i]}_{p\text{-}DTD}(t)$ decays by the factor of $1/\beta_{f\text{-}DTD}(t^*) = 0.4$) and the hierarchy is not so clear. However, of course, this scenario is not valid because the full-DTD picture does not hold for CT-PI (cf. Figure 4).

Finally, it is also informative to compare the hypothetical stress decay function due only to CR, $\psi_{CR}(t)$ ($= 1/\beta_{CR}(t)$), for chains having different topological architectures (cf. schematic illustration shown in Figure 9). For free and tethered linear chains each composed of N segments, the Rouse-CR mechanism (in the continuous limit) gives the ratio r_p of the relaxation time τ_1 ($= 2\tau_G^{CR}$) of the slowest CR mode to τ_p of pth mode as

$$r_p \equiv \frac{\tau_1}{\tau_p} = p^2 \quad \text{with } \tau_1 = \frac{\zeta_{CR}}{2\kappa}\left(\frac{N}{\pi}\right)^2 \text{ (for free linear chain)} \quad (13a)$$

$$r_p = (2p-1)^2 \quad \text{with } \tau_1 = \frac{\zeta_{CR}}{2\kappa}\left(\frac{2N}{\pi}\right)^2 \text{ (for tethered linear chain)} \quad (13b)$$

For the tethered/bifurcated chain with $N_i = 2N_o$ (model for our CT-PI), this ratio has been specified by eqs 11a–11c. For all these chains, the stress decay function is expressed as $\psi_{CR}(t) = N^{-1}\sum_{p=1}^{N} \exp(-r_p t/\tau_1)$, where N is the total number of the CR modes that corresponds to the total number of the entanglement segments per chain. (In this expression, we have neglected the contribution from the intrinsic Rouse fluctuation explained earlier.)

For examination of an effect(s) of the chain architecture on the CR mode distribution, Figure 9 compares $\psi_{CR}(t)$ for the free and tethered linear chains having the same N (= 60) and

the tethered/bifurcated chain having the same half-span as the tethered linear chain, $N_i + N_o = N = 60$ ($N_i = 40$ and $N_o = 20$). $\psi_{CR}(t)$ is plotted against a reduced time, t/τ_ζ, where τ_ζ ($= \zeta_{CR}/2\kappa\pi^2$) represents the local CR hopping time. (Thus, the behavior of the chains is compared at an *effectively* isofrictional state.) Clearly, $\psi_{CR}(t)$ begins to decay at $t \simeq \tau_\zeta$ for all chains. This early stage decay behavior does not depend on the chain architecture because the local motion is generally insensitive to the global architecture. However, at longer t, the decay of $\psi_{CR}(t)$ is slower in the order of tethered/bifurcated > tethered linear > free linear, the former two having the same half-span length ($N = 60$). We also note that the range of t where the asymptotic power-law behavior ($\psi_{CR}(t) \propto t^{-1/2}$) prevails is wider in this order. Even larger differences are expected if the chain has more complicatedly multibranched structure. Thus, the slow CR mode distribution of the chains varies considerably with their topological architectures characterized by the branching functionality, branch length distribution, and so on.

Some of the current molecular models for multibranched chains[29,31] correctly incorporate the partial-DTD mechanism (or a similar mechanism) into the hierarchical relaxation scheme. However, these models do not seem to have properly considered the change of the DTD behavior with the chain architecture demonstrated above: For the case of CR-governed partial-DTD, the dilated tube diameter is given by $a'(t) = a\{\psi_{CR}(t)\}^{-1/2}$, and thus DTD is slower for tethered/bifurcated chains than for linear chains if these chains have the same local CR hopping time (cf. Figure 9). The models could be further refined by adequately incorporating this change.

4. Concluding Remarks

For the entangled Cayley-tree-type *cis*-polyisoprene (CT-PI) composed of trifunctionally branched inner arms each having two outer arms ($M_i = 24.7 \times 10^3$ and $M_o = 12.3 \times 10^3$), the molecular picture of dynamic tube dilation (DTD) was examined experimentally through comparison of the viscoelastic and dielectric data. The type A dipoles of CT-PI enabled us to unequivocally determine the survival fraction of the dilated tube $\varphi'(t)$ from the dielectric data. The full-DTD picture regards the relaxed portions of chains as a simple solvent to give a relationship between $\varphi'(t)$ and the normalized viscoelastic relaxation function, $\mu_{f\text{-}DTD}(t) = \{\varphi'(t)\}^{1+d}$ with $d = 1.3$ (for PI). This relationship was found to fail for CT-PI. In contrast, the partial-DTD picture considers the consistency of DTD and the constraint release (CR) mechanisms to give a relationship $\mu_{p\text{-}DTD}(t) = \varphi'(t)/\beta^*(t)$ with $\beta^*(t) = \min[\beta_{f\text{-}DTD}(t), \beta_{CR}(t)]$, where $\beta_{f\text{-}DTD}(t) = \{\varphi'(t)\}^{-d}$ and $\beta_{CR}(t)$ is the maximum possible number of the entanglement segments that can be mutually CR-equilibrated in a given time scale, t. This partial-DTD relationship was found to hold satisfactorily for the $\varphi'(t)$ and $\mu(t)$ data. These results were in harmony with those found for star-branched PI chains, suggesting that the consistent coarse-graining of the length and time scales on the basis of the CR mechanism is particularly important for description of the branched chain dynamics. Analysis of the $\varphi'(t)$ data suggested that our CT-PI exhibits the hierarchical relaxation from the outer arms to inter arms through the partial-DTD mechanism.

We also noted that the hypothetical stress decay function due only to CR, $\psi_{CR}(t)$ ($= 1/\beta_{CR}(t)$), changes with the topological architecture of the chain. Specifically, the CR relaxation at long t was found to be slower for tethered/bifurcated chains than for linear chains having the same local CR hopping time, given that the former has the half-span length being identical to the total chain length of the latter. Consideration of this change would be helpful for refining the current molecular models for multibranched chains.

Acknowledgment. This work was partly supported by Grant-in-Aid for Scientific Research on Priority Area "Soft Matter Physics" from the Ministry of Education, Culture, Sports, Science and Technology, Japan (grant #18068009) and by the EU (NoE Softcomp, NMP3-CT-2004-502235).

Appendix A. Formulation of Relationship between $\Phi(t)$ and $\varphi'(t)$ for CT-PI

The averages of the end-to-end vectors of the inner/outer arms of the CT-PI chain appearing in eq 6, $\langle \mathbf{R}_\alpha(t)\cdot\mathbf{R}_\beta(0)\rangle$ (α, β = i, o1, o2), are contributed from the cross-correlation between $\mathbf{R}_\beta(0)$ and the displacements $\mathbf{D}$. The relationship between the dielectric $\Phi(t)$ and the tube survival fraction $\varphi'(t)$, derived from analysis of this contribution, is explained below, first for the early stage of relaxation and then for the late stage.

A.1. Early Stage. In Figure 1b, the thick dashed curve illustrates the conformation the group of arms at time 0. At a time t in the early stage of relaxation, the dilated tube constrains the whole entanglement segments of the inner arm and a fraction $\varphi_o'(t)$ of the outer arm segments, as illustrated with the thick solid curve. Considering a change of the chain conformation in the interval of time from 0 to t, we can express the end-to-end vectors of the arms at time t, $\mathbf{R}_\alpha(t)$ (α = i, o1, o2), in terms of the vectors at time 0, $\mathbf{R}_\alpha(0)$, and the displacements $\mathbf{D}$ (cf. Figure 1b) to formulate a relationship between $\Phi(t)$ (eq 6) and $\varphi'(t)$ (eq 7), as explained below.

In this interval, the outer branching point (= outer end of the inner arm) exhibits a displacement $\mathbf{D}_i$ (see Figure 1b), and $\mathbf{R}_i(t)$ of this arm at the time t is given by

$$\mathbf{R}_i(t) = \mathbf{R}_i(0) + \mathbf{D}_i \tag{A1}$$

The portion of the kth outer arm (k = 1, 2) in the surviving tube exhibits this displacement $\mathbf{D}_i$ as well as a displacement $\mathbf{D}_{ok}$ at the tube edge (cf. Figure 1b). Thus, the end-to-end vector $\mathbf{r}_{ok}$ of this portion at time t is written as

$$\mathbf{r}_{ok}(t) = \mathbf{r}_{ok}(0) + \mathbf{D}_{ok} - \mathbf{D}_i \quad (k = 1, 2) \tag{A2}$$

Since the initial orientational memory is preserved only in the surviving tube, we can utilize eqs A1 and A2 to rewrite eq 6 as

$$\Phi(t) = \frac{\langle\{\mathbf{R}_i(0) + \mathbf{r}_{o1}(0) + \mathbf{r}_{o2}(0) + \mathbf{D}_{o1} + \mathbf{D}_{o2} - \mathbf{D}_i\}\cdot\{\mathbf{R}_i(0) + \mathbf{r}_{o1}(0) + \mathbf{r}_{o2}(0)\}\rangle}{(N_i + 2N_o)a^2} \tag{A3}$$

From the Gaussian feature of the portions of the inner and outer arms in the surviving tube, we find relationships $\langle\{\mathbf{R}_i(0)\}^2\rangle = N_i a^2$, $\langle \mathbf{R}_i(0)\cdot\mathbf{r}_{ok}(0)\rangle = 0$, and $\langle \mathbf{r}_{ok}(0)\cdot\mathbf{r}_{oq}(0)\rangle = \delta_{kq} a^2 N_o \varphi_o'(t)$ where δ_{kq} is Kronecker delta and $N_o\varphi_o'(t)$ is the number of the entanglement segments of the outer arm in the surviving tube. Utilizing these relationships in eq A3 and considering the expression of $\varphi'(t)$ in the early stage, $\varphi'(t) = \{N_i + 2N_o\varphi_o'(t)\}/\{N_i + 2N_o\}$ (eq 7), we find

$$\Phi(t) = \varphi'(t) + \frac{\langle\{\mathbf{D}_{o1} + \mathbf{D}_{o2} - \mathbf{D}_i\}\cdot\{\mathbf{R}_i(0) + \mathbf{r}_{o1}(0) + \mathbf{r}_{o2}(0)\}\rangle}{(N_i + 2N_o)a^2} \tag{A4}$$

The second term in the right-hand side of eq A4 can be evaluated from eqs A1 and A2. Since $\langle\{\mathbf{R}_i(t)\}^2\rangle = \langle\{\mathbf{R}_i(0)\}^2\rangle$ and $\langle\{\mathbf{r}_{ok}(t)\}^2\rangle = \langle\{\mathbf{r}_{ok}(0)\}^2\rangle$ for the Gaussian CT-PI chain at equilibrium, we can compare mean-square averages of both sides of eqs A1 and A2 to find relationships, $2\langle\mathbf{R}_i(0)\cdot\mathbf{D}_i\rangle = -\langle\mathbf{D}_i^2\rangle$ and $2\langle\mathbf{r}_{ok}(0)\cdot\{\mathbf{D}_{ok} - \mathbf{D}_i\}\rangle = -\langle\mathbf{D}_i^2\rangle - \langle\mathbf{D}_{ok}^2\rangle + 2\langle\mathbf{D}_i\cdot\mathbf{D}_{ok}\rangle$. Furthermore, we can add eqs A1 and A2 and/or subtract eq A2 with k = 1 from eq A2 with k = 2 to obtain equations not including $\mathbf{D}_i$. From mean-square averages of both sides of these

equations, we similarly find the other set of relationships, $2\langle\{\mathbf{R}_i(0)+\mathbf{r}_{ok}(0)\}\cdot\mathbf{D}_{ok}\rangle=-\langle\mathbf{D}_{ok}^2\rangle$ and $2\langle\{\mathbf{r}_{o1}(0)-\mathbf{r}_{o2}(0)\}\cdot\{\mathbf{D}_{o1}-\mathbf{D}_{o2}\}\rangle=-\langle\mathbf{D}_{o1}^2\rangle-\langle\mathbf{D}_{o2}^2\rangle+2\langle\mathbf{D}_{o1}\cdot\mathbf{D}_{o2}\rangle$. Substituting all these relationships in eq A4, we find

$$\Phi(t)=\varphi'(t)+\frac{\left\{-\frac{3}{2}\langle\mathbf{D}^2\rangle+\langle\mathbf{D}_{o1}\cdot\mathbf{D}_i\rangle+\langle\mathbf{D}_{o2}\cdot\mathbf{D}_i\rangle-\langle\mathbf{D}_{o1}\cdot\mathbf{D}_{o2}\rangle\right\}}{(N_i+2N_o)a^2} \tag{A5}$$

The dilated tube is considered to have a uniform diameter along the chain backbone. Thus, in eq A5, the averages $\langle\mathbf{D}_{ok}^2\rangle$ ($k=1$ and 2) and $\langle\mathbf{D}_i^2\rangle$ have been set equal to each other and simply denoted as $\langle\mathbf{D}^2\rangle$. This $\langle\mathbf{D}^2\rangle$ can be evaluated as a mean-square distance of two entanglement segments (of the diameter a) randomly located on a circular cross section/edge of the dilated tube of the diameter $a'(t)$:[10,37] $\langle\mathbf{D}^2\rangle=\{a'(t)-a\}^2/4$. (In our treatment utilizing the entanglement segment as the local structural unit, the displacement occurs only when the tube dilates to provide this segment with the freedom of lateral motion, i.e., $\langle\mathbf{D}^2\rangle>0$ only when $a'(t)>a$.)

Equation A5 includes the cross-correlation terms for the displacements of different segments, $\langle\mathbf{D}_{o1}\cdot\mathbf{D}_i\rangle$, $\langle\mathbf{D}_{o2}\cdot\mathbf{D}_i\rangle$, and $\langle\mathbf{D}_{o1}\cdot\mathbf{D}_{o2}\rangle$. Evaluation of these terms requires us to specify the chain dynamics, which is different from the situation for $\langle\mathbf{D}^2\rangle$ (being directly related to $a'(t)$.) As an example, the cross-correlation terms for the Rouse constraint release (CR) dynamics are calculated in Appendix B. Of course, details of these terms change with the chain dynamics. However, we also note a general feature that the cross-correlation grows with time irrespective of the chain dynamics. Namely, the $\langle\mathbf{D}_{o1}\cdot\mathbf{D}_{o2}\rangle$ and $\langle\mathbf{D}_{ok}\cdot\mathbf{D}_i\rangle$ ($k=1$, 2) terms are small compared to $\langle\mathbf{D}^2\rangle$ at short t where the tube hardly dilates, while they approach $\langle\mathbf{D}^2\rangle$ on an increase of t up to the tube escape time of the outer arm, t^*. (At $t=t^*$, the entanglement segments on the tube edges coincide with the segment at the outer branching point and thus $\langle\mathbf{D}_{ok}\cdot\mathbf{D}_i\rangle=\langle\mathbf{D}_{o1}\cdot\mathbf{D}_{o2}\rangle=\langle\mathbf{D}_i^2\rangle=\langle\mathbf{D}^2\rangle$.) Thus, we may generally express the cross-correlation terms as $\langle\mathbf{D}_{ok}\cdot\mathbf{D}_i\rangle=\langle\mathbf{D}^2\rangle Q_{oi}(t)$ and $\langle\mathbf{D}_{o1}\cdot\mathbf{D}_{o2}\rangle=\langle\mathbf{D}^2\rangle Q_{oo}(t)$, where $Q_{oi}(t)$ and $Q_{oo}(t)$ are functions that increase with t and satisfy the condition $Q_{oi}(t^*)=Q_{oo}(t^*)=1$. Since the contour distance between the outer branching point and the segment on the dilated tube edge is smaller than the distance between the two segments on the different edges (cf. Figure 1b), we generally expect $Q_{oi}(t)\geq Q_{oo}(t)$.

Substituting the above expressions of $\langle\mathbf{D}_{ok}\cdot\mathbf{D}_i\rangle$, $\langle\mathbf{D}_{o1}\cdot\mathbf{D}_{o2}\rangle$, and $\langle\mathbf{D}^2\rangle$ in eq A5, we finally obtain the relationship between the tube survival fraction $\varphi'(t)$ and the dielectric $\Phi(t)$ of CT-PI:

$$\Phi(t)=\varphi'(t)-\frac{3}{8(N_i+2N_o)}\left\{\frac{a'(t)}{a}-1\right\}^2\left\{1-\frac{4}{3}Q_{oi}(t)+\frac{2}{3}Q_{oo}(t)\right\}\quad\text{for } N_o>\beta(t) \text{ and } \varphi'(t)>v_i\ (t<t^*) \tag{A6}$$

This equation is identical to eq 8 in the text. Note that eq A6 has a sound meaning only when (1) N_o is larger than the number $\beta(t)$ of entanglement segments per dilated segment so that the outer arm is composed of more than one dilated segment and (2) $\varphi'(t)$ is larger than the volume fraction v_i of the inner arm so that the outer arm has not fully escaped from the dilated tube ($t<t^*$).

A.2. Late Stage. In the late stage of relaxation where $N_o<\beta(t)$ and/or $\varphi'(t)<v_i$ ($t>t^*$), only a fraction $\varphi_i'(t)$ of the inner arm segments remains in the surviving part of the dilated tube and $\varphi'(t)$ coincides with $N_i\varphi_i'(t)/(N_i+2N_o)$. For this case, eq 6 reduces to

$$\Phi(t)=\frac{\langle\mathbf{r}_i(t)\cdot\mathbf{r}_i(0)\rangle}{(N_i+2N_o)a^2}=\frac{\langle\{\mathbf{r}_i(0)+\mathbf{D}_i'\}\cdot\mathbf{r}_i(0)\rangle}{(N_i+2N_o)a^2} \tag{A7}$$

Here, $\mathbf{r}_i(0)$ and $\mathbf{r}_i(t)$ ($=\mathbf{r}_i(0)+\mathbf{D}_i'$) denote the end-to-end vector at times 0 and t defined for the portion of the inner arm in the surviving tube, and $\mathbf{D}_i'$ is a displacement of this portion at the edge of this tube in the interval of time from 0 to t. Since this portion is composed of $N_i\varphi_i'(t)$ entanglement segments, $\langle\{\mathbf{r}_i(0)\}^2\rangle=N_i\varphi_i'(t)a^2$. We also find a relationship, $\langle\mathbf{D}_i'\cdot\mathbf{r}_i(0)\rangle=-\langle(\mathbf{D}_i')^2\rangle/2=-\{a'(t)-a\}^2/8$, from the mean-square averages of both sides of the equation, $\mathbf{r}_i(t)=\mathbf{r}_i(0)+\mathbf{D}_i'$. Thus, we finally obtain

$$\Phi(t)=\varphi'(t)-\frac{1}{8(N_i+2N_o)}\left\{\frac{a'(t)}{a}-1\right\}^2\quad\text{for } \beta(t)<N_i+2N_o \text{ and } 1/(N_i+2N_o)<\varphi'(t)<v_i \tag{A8}$$

This equation is identical to eq 9 in the text. Note that eq A8 loses its sound meaning when the inner arm and two outer arms attached thereto are equilibrated as a whole ($\beta(t)>N_i+2N_o$) and/or less than one entanglement segment remains in the dilated tube ($(N_i+2N_o)\varphi'(t)<1$). Note also that the cross-correlation functions ($Q_{oi}(t)$ and $Q_{oo}(t)$ in eq A6) do not appear in eq A8 because the surviving portion of the dilated tube has just one edge in the range of t where eq A8 is formulated.

Appendix B. Rouse-CR Eigenmode Analysis for Tethered and Bifurcated Chain

B.1. Eigenmode Amplitudes. The M_i/M_o ratio of our CT-PI chain is very close to 2. Thus, for analysis of its Rouse-type constraint release (CR) behavior, we model this chain as a tethered and bifurcated bead−spring chain composed of three arms: a tethered inner arm having $N_i=2N_o$ beads (each bead corresponds to the entanglement segment) and two outer arms each having N_o beads. Two outer arms are indexed with $j=1$ and 2, and the inner arm is indexed with $j=3$. The bead coordinate n in the inner and outer arms runs from 0 to $2N_o$ and N_o, respectively, with the branching point connecting these arms being chosen to be the hypothetical zeroth bead common to all arms. Each bead has the friction coefficient ζ_{CR} corresponding to a local CR hopping time,[2] except the zeroth bead that is considered to be frictionless. Neighboring beads are connected with a spring of strength $\kappa=3k_BT/a^2$, with a and k_B being the equilibrium size of the entanglement segment and Boltzmann constant, respectively.

We consider the Rouse-CR dynamics in the continuous limit. Then, the spatial position of nth bead in jth arm at time t, $\mathbf{r}^{[j]}(n,t)$, obeys the standard Rouse equation of motion[3,4]

$$\zeta_{CR}\frac{\partial\mathbf{r}^{[j]}(n,t)}{\partial t}=\kappa\frac{\partial^2\mathbf{r}^{[j]}(n,t)}{\partial n^2}+\mathbf{f}^{[j]}(n,t)\quad(j=1-3) \tag{B1}$$

where $\mathbf{f}^{[j]}(n,t)$ represents the Brownian force acting on nth bead in jth arm. This $\mathbf{f}^{[j]}(n,t)$ is modeled as the white noise having the dyadic average[3,4]

$$\langle\mathbf{f}^{[j]}(n,t)\,\mathbf{f}^{[i]}(n',t')\rangle=2\zeta_{CR}k_BT\delta(n-n')\,\delta(t-t')\delta_{ji}\mathbf{I} \tag{B2}$$

where $\mathbf{I}$ is the unit tensor.

The boundary condition for eq B1 is given by

$$\frac{\partial\mathbf{r}^{[1]}(n,t)}{\partial n}=\frac{\partial\mathbf{r}^{[2]}(n,t)}{\partial n}=\mathbf{0}\quad\text{for } n=N_o \tag{B3}$$

$$\mathbf{r}^{[3]}(2N_o,t)=\mathbf{0} \tag{B4}$$

$$\sum_{j=1}^{3}\left\{\frac{\partial\mathbf{r}^{[j]}(n,t)}{\partial n}\right\}_{n=0}=\mathbf{0} \tag{B5}$$

Equation B3 indicates lack of external force acting on the free ends of the outer arms, and eq B4 means that the inner arm is

tethered to the origin **0** of the spatial coordinate system. Equation B5 represents the balance of tensions of the three arms at the branching point (= zeroth bead common to three arms). Equations B3 and B5 are identical to the boundary condition utilized in the Zimm−Kilb model[45] for star chains.

From eqs B1 and B3–B5, $\mathbf{r}^{[j]}(n,t)$ can be expanded into series of eigenmodes indexed with the mode number k:

$$\mathbf{r}^{[j]}(n,t) = \sum_{k\geq 0}\left[\mathbf{A}_k^{[j]}(t)\,\sin\left\{\frac{\xi_k n}{N_o}\right\} + 2\,\sin\lambda_k\,\mathbf{B}_k(t)\,\cos\left(\frac{\lambda_k(N_o-n)}{N_o}\right)\right] \quad (j=1,2) \tag{B6}$$

$$\mathbf{r}^{[3]}(n,t) = \sum_{k\geq 0}\left[-\left\{\mathbf{A}_k^{[1]}(t)+\mathbf{A}_k^{[2]}(t)\right\}\sin\left\{\frac{\xi_k n}{N_o}\right\} + \mathbf{B}_k(t)\,\sin\left(\frac{\lambda_k(2N_o-n)}{N_o}\right)\right] \tag{B7}$$

with

$$\xi_k = \frac{(2k+1)\pi}{2} \quad (k=0,1,2,...) \tag{B8}$$

The eigenmode amplitudes ($\mathbf{A}$, $\mathbf{B}$) are not totally independent for the three arms because of the boundary condition, eq B5, and the chain connectivity requirement ($\mathbf{r}^{[1]}(0,t) = \mathbf{r}^{[2]}(0,t) = \mathbf{r}^{[3]}(0,t)$). This fact has been considered in eqs B6 and B7 in the following way.

For the eigenmodes activating no motion of the branching/bifurcation point and thus having the node at $n = 0$ (referred to as *A modes*), the amplitudes for the outer two arms, $\mathbf{A}_k^{[j]}(t)$ with $j = 1, 2$, have been chosen as the variables in eqs B6 and B7. ($\mathbf{A}_k^{[3]}(t) = -\{\mathbf{A}_k^{[1]}(t) + \mathbf{A}_k^{[2]}(t)\}$; cf. eq B5.) These A modes, having the eigenvalues ξ_k (eq B8), are dually *degenerated* because the two outer arms are equivalent to each other, as similar to the situation for regular star-branched chains.[45] It should be also noted that the A modes are allowed for our tethered/branched chain because it has the integer ratio, $N_i/N_o = 2$. Such modes are prohibited in general cases of nonrationalized N_i/N_o ratio. Thus, the N_i/N_o ratio is very important in the calculation of the eigenmodes. For this reason, we have faithfully transferred the M_i/M_o ratio of our CT-PI (being very close to 2) to the N_i/N_o ratio in the eigenmode calculation.

For the eigenmodes activating the motion of the branching/bifurcation point (referred to as *B modes*), the three arms move in a fully correlated way and only the mode amplitude for a particular arm behaves as the independent amplitude. In eqs B6 and B7, we have chosen the amplitude of the inner arm, $\mathbf{B}_k(t)$, as this independent amplitude. (The amplitudes of the two outer arms, $\mathbf{B}_k^{[1]}(t)$ and $\mathbf{B}_k^{[2]}(t)$, are given by $2\,\sin\lambda_k\,\mathbf{B}_k(t)$ because of the chain connectivity.) From eq B5, the eigenvalues λ_k for the B modes are determined as

$$\sin^2\lambda_k = \frac{1}{6} \quad (0<\lambda_0<\lambda_1<\lambda_2\ ...) \tag{B9}$$

These eigenvalues split into two series

$$\lambda_{k,+} = k\pi+\theta \quad \text{and} \quad \lambda_{k,-} = (k+1)\pi-\theta \quad (k=0,1,2,...) \tag{B10}$$

with

$$\theta = \sin^{-1}\left(\frac{1}{\sqrt{6}}\right) \quad (=0.13386\pi) \tag{B11}$$

Correspondingly, the amplitudes for the inner arm also split into two series, $\mathbf{B}_{k,\alpha}$ indexed with $\alpha = +$ and $-$.

Thus, the whole set of eigenmodes splits into four series, the two series of dually degenerated A modes and the two series of B modes, the latter having the nondegenerated eigenvalues $\lambda_{k,\alpha}$ ($\alpha = +$ and $-$; cf. eq B10). The eigenfunctions for these modes satisfy the orthogonality relationships

$$\int_0^{N_o}\sin\left\{\frac{\xi_p n}{N_o}\right\}\sin\left\{\frac{\xi_q n}{N_o}\right\}dn = \frac{N_o}{2}\delta_{pq} \tag{B12}$$

$$\int_0^{N_o}\sin\left\{\frac{\xi_p n}{N_o}\right\}\left[2\,\sin\lambda_{q,\alpha}\,\cos\left\{\frac{\lambda_{q,\alpha}(N_o-n)}{N_o}\right\}\right]dn - \int_0^{2N_o}\sin\left\{\frac{\xi_p n}{N_o}\right\}\sin\left\{\frac{\lambda_{q,\alpha}(2N_o-n)}{N_o}\right\}dn = 0 \quad \text{for any } p,q,\alpha \tag{B13}$$

$$2\int_0^{N_o}\left[2\,\sin\lambda_{p,\alpha}\,\cos\left\{\frac{\lambda_{p,\alpha}(N_o-n)}{N_o}\right\}\right]\times\left[2\,\sin\lambda_{q,\beta}\,\cos\left\{\frac{\lambda_{q,\beta}(N_o-n)}{N_o}\right\}\right]dn + \int_0^{2N_o}\sin\left\{\frac{\lambda_{p,\alpha}(2N_o-n)}{N_o}\right\}\times\sin\left\{\frac{\lambda_{q,\beta}(2N_o-n)}{N_o}\right\}dn = \frac{5N_o}{3}\delta_{pq}\delta_{\alpha\beta} \tag{B14}$$

Applying these relationships to eqs B6 and B7, we find a time-evolution equation for each of the eigenmode amplitudes, $\mathbf{A}_k^{[j]}(t)$ and $\mathbf{B}_{k,\alpha}(t)$, that can be solved with the standard method.[3,4] The solutions for arbitrary initial amplitudes, $\mathbf{A}_k^{[j]}(0)$ ($j = 1, 2$) and $\mathbf{B}_{k,\alpha}(0)$ ($\alpha = +, -$), can be summarized as

$$\mathbf{A}_k^{[j]}(t) = \mathbf{A}_k^{[j]}(0)\,\exp\left(-\frac{\kappa{\xi_k}^2}{{N_o}^2\zeta_{CR}}t\right) + \frac{1}{5N_o\zeta_{CR}}\int_0^t\exp\left(-\frac{\kappa{\xi_k}^2}{{N_o}^2\zeta_{CR}}(t-t')\right)\times\left\{\sum_{i=1}^{3}X_{ji}\int_0^{N_o}\sin\left(\frac{\xi_k n}{N_o}\right)\mathbf{f}^{[i]}(n,t')\,dn\right\}dt' \tag{B15}$$

with $X_{11} = 6$, $X_{12} = -4$, $X_{13} = -2$, $X_{21} = -4$, $X_{22} = 6$, $X_{23} = -2$, and

$$\mathbf{B}_{k,\alpha}(t) = \mathbf{B}_{k,\alpha}(0)\,\exp\left(-\frac{\kappa{\lambda_{k,\alpha}}^2}{{N_o}^2\zeta_{CR}}t\right) + \frac{3}{5N_o\zeta_{CR}}\int_0^t\exp\left(-\frac{\kappa{\lambda_{k,\alpha}}^2}{{N_o}^2\zeta_{CR}}(t-t')\right)\times\left\{2\,\sin\lambda_{k,\alpha}\int_0^{N_o}\cos\left(\frac{\lambda_{k,\alpha}(N_o-n)}{N_o}\right)[\mathbf{f}^{[1]1}(n,t')+\mathbf{f}^{[2]1}(n,t')]\,dn + \int_0^{2N_o}\sin\left(\frac{\lambda_{k,\alpha}(2N_o-n)}{N_o}\right)\mathbf{f}^{[3]1}(n,t')\,dn\right\}dt' \tag{B16}$$

Applying eq B2 to these solutions, we can further calculate the dyadic averages of the amplitudes at time t. The results are summarized as

$$\left\langle\mathbf{A}_p^{[j]}(t)\,\mathbf{A}_q^{[j]}(t)\right\rangle = \left\langle\mathbf{A}_p^{[j]}(0)\,\mathbf{A}_p^{[j]}(0)\right\rangle\exp\left(-\frac{\kappa\left({\xi_p}^2+{\xi_q}^2\right)}{{N_o}^2\zeta_{CR}}t\right) + \mathbf{I}\delta_{pq}\left(\frac{2N_o a^2}{5{\xi_p}^2}\right)\left\{1-\exp\left(-\frac{2\kappa{\xi_p}^2}{{N_o}^2\zeta_{CR}}t\right)\right\} \quad (j=1,2) \tag{B17}$$

$$\left\langle\mathbf{A}_p^{[1]1}(t)\,\mathbf{A}_q^{[2]1}(t)\right\rangle = \left\langle\mathbf{A}_p^{[1]1}(0)\,\mathbf{A}_q^{[2]1}(0)\right\rangle\exp\left(-\frac{\kappa\left({\xi_p}^2+{\xi_q}^2\right)}{{N_o}^2\zeta_{CR}}t\right) - \mathbf{I}\delta_{pq}\left(\frac{4N_o a^2}{15{\xi_p}^2}\right)\left\{1-\exp\left(-\frac{2\kappa{\xi_p}^2}{{N_o}^2\zeta_{CR}}t\right)\right\} \tag{B18}$$

$$\langle \mathbf{A}_p(t)\, \mathbf{B}_{q,\beta}(t)\rangle = \langle \mathbf{A}_p(0)\, \mathbf{B}_{q,\beta}(0)\rangle \exp\left(-\frac{\kappa(\xi_p^{\,2}+\lambda_{q,\beta}^{\,2})}{N_o^{\,2}\zeta_{CR}}t\right) \tag{B19}$$

$$\langle \mathbf{B}_{p,\alpha}(t)\, \mathbf{B}_{q,\beta}(t)\rangle = \langle \mathbf{B}_{p,\alpha}(0)\, \mathbf{B}_{q,\beta}(0)\rangle \exp\left(-\frac{\kappa(\lambda_{p,\alpha}^{\,2}+\lambda_{q,\beta}^{\,2})}{N_o^{\,2}\zeta_{CR}}t\right) + \mathbf{I}\delta_{pq}\delta_{\alpha\beta}\left(\frac{N_o a^2}{5\lambda_{p,\alpha}^{\,2}}\right)\left\{1-\exp\left(-\frac{2\kappa\lambda_{p,\alpha}^{\,2}}{N_o^{\,2}\zeta_{CR}}t\right)\right\} \tag{B20}$$

Full equilibration is attained at sufficiently long t irrespective of the initial condition. Thus, eqs B17–B20 with $t = \infty$ give the averages at equilibrium:

$$\left\langle \mathbf{A}_p^{[j1]}\, \mathbf{A}_q^{[j1]}\right\rangle_{eq} = \mathbf{I}\delta_{pq}\left(\frac{2N_o a^2}{5\xi_p^{\,2}}\right) \quad (j=1,2) \tag{B21}$$

$$\left\langle \mathbf{A}_p^{[11]}\, \mathbf{A}_q^{[21]}\right\rangle_{eq} = -\mathbf{I}\delta_{pq}\left(\frac{4N_o a^2}{15\xi_p^{\,2}}\right) \tag{B22}$$

$$\langle \mathbf{A}_p \mathbf{B}_{q,\beta}\rangle_{eq} = \mathbf{0} \quad \text{for any } p,q,\beta\ (=+ \text{ and } -) \tag{B23}$$

$$\langle \mathbf{B}_{p,\alpha}\mathbf{B}_{q,\beta}\rangle_{eq} = \mathbf{I}\delta_{pq}\delta_{\alpha\beta}\left(\frac{N_o a^2}{5\lambda_{p,\alpha}^{\,2}}\right) \tag{B24}$$

These equilibrium averages are utilized in the calculation of the segment displacement and viscoelastic relaxation function explained below.

B.2. Segment Displacement. We consider a range of time where the outer arm has not fully escaped from the dilated tube and the survival fraction of the tube for this arm is given by φ_o' (>0); cf. Figure 1b. At a time t in this range, $N_o\varphi_o' th$ segment of the jth outer arm is located on the edge of the surviving portion of the dilated tube. The displacement of this segment in an interval of time from 0 to t, $\mathbf{D}_{oj}$ (j = 1, 2) is written as (cf. eq B6)

$$\begin{aligned}\mathbf{D}_{oj} &= \mathbf{r}^{[j1]}(N_o\varphi_o', t) - \mathbf{r}^{[j1]}(N_o\varphi_o', 0)\\ &= \sum_{k\ge 0}\{\mathbf{A}_k^{[j1]}(t) - \mathbf{A}_k^{[j1]}(0)\}\sin\xi_k\varphi_o' + \\ &\sum_{\alpha=+,-}\sum_{k\ge 0}[2\sin\lambda_{k,\alpha}\{\mathbf{B}_{k,\alpha}(t) - \mathbf{B}_{k,\alpha}(0)\}\cos\lambda_{k,\alpha}(1-\varphi_o')]\end{aligned} \quad (j=1,2) \tag{B25}$$

Similarly, the displacement of the branching/bifurcation point, $\mathbf{D}_i$, is given by (cf. eq B7)

$$\mathbf{D}_i = \mathbf{r}^{[31]}(0,t) - \mathbf{r}^{[31]}(0,0) = \sum_{\alpha=+,-}\sum_{k\ge 0}\{\mathbf{B}_{k,\alpha}(t) - \mathbf{B}_{k,\alpha}(0)\}\sin 2\lambda_{k,\alpha} \tag{B26}$$

From the general expressions of the eigenmode amplitudes $\mathbf{A}_k^{[j]}(t)$ and $\mathbf{B}_{k,\alpha}(t)$ (eqs B15 and B16) together with the dyadic averages at equilibrium (eqs B21–B24), we can obtain expressions of the equilibrium mean-square displacement of the branching/bifurcation point, $\langle \mathbf{D}_i^2\rangle$, as well as the equilibrium cross-correlations of the displacements defined for this point and the segments on the dilated tube edges, $\langle \mathbf{D}_i\cdot\mathbf{D}_{oj}\rangle$ and $\langle \mathbf{D}_{o1}\cdot\mathbf{D}_{o2}\rangle$. The results are summarized as

$$\langle \mathbf{D}_i^2\rangle = \left(\frac{2N_o a^2}{3}\right)\sum_{\alpha=+,-}\sum_{k\ge 0}\frac{1}{\lambda_{k,\alpha}^{\,2}}\left\{1-\exp\left(-\frac{\kappa\lambda_{k,\alpha}^{\,2}}{N_o^{\,2}\zeta_{CR}}t\right)\right\} \tag{B27}$$

$$\langle \mathbf{D}_i\cdot\mathbf{D}_{oj}\rangle = \left(\frac{4N_o a^2}{5}\right)\sum_{\alpha=+,-}\sum_{k\ge 0}\frac{\cos\lambda_{k,\alpha}\cos\lambda_{k,\alpha}(1-\varphi_o')}{\lambda_{k,\alpha}^{\,2}}\times \left\{1-\exp\left(-\frac{\kappa\lambda_{k,\alpha}^{\,2}}{N_o^{\,2}\zeta_{CR}}t\right)\right\} \tag{B28}$$

$$\langle \mathbf{D}_{o1}\cdot\mathbf{D}_{o2}\rangle = -\left(\frac{8N_o a^2}{5}\right)\sum_{k\ge 0}\frac{\sin^2\xi_k\varphi_o'}{\xi_k^{\,2}}\left\{1-\exp\left(-\frac{\kappa\xi_k^{\,2}}{N_o^{\,2}\zeta_{CR}}t\right)\right\} + \left(\frac{4N_o a^2}{5}\right)\sum_{\alpha=+,-}\sum_{k\ge 0}\frac{\cos^2\lambda_{k,\alpha}(1-\varphi_o')}{\lambda_{k,\alpha}^{\,2}}\left\{1-\exp\left(-\frac{\kappa\lambda_{k,\alpha}^{\,2}}{N_o^{\,2}\zeta_{CR}}t\right)\right\} \tag{B29}$$

The time evolution of the square-displacements given by eqs B27–B29 can be specified in the following way. The survival fraction of the dilated tube for the outer arm included in eqs B27–B29, $\varphi_o'(t)$, is related to the average survival fraction $\varphi'(t)$ as $\varphi_o' = (2N_o + N_i)\varphi'/2N_o - N_i/2N_o$ (eq 7). This $\varphi_o'(t)$ decreases to 0 on the decrease of $\varphi'(t)$ to the inner arm volume fraction $v_i = N_i/(2N_o + N_i)$, i.e., on the increase of t up to the tube escape time of the outer arm, t^* (= 2.5×10^{-3} s; cf. Figure 5). For our CT-PI, the upper and lower bound values of $\varphi'(t)$ at $t < t^*$ differed only by less than 2%, as explained for Figure 5. Thus, to a very good approximation, we may replace φ_o' included in eqs B27–B29 by $\varphi_o'' = (2N_o + N_i)\Phi(t)/2N_o - N_i/2N_o$, where $\Phi(t)$ is the dielectric relaxation function being identical to the lower bound of $\varphi'(t)$. The longest retardation time appearing in eqs B27–B29, $N_o^2\zeta_{CR}/\kappa\lambda_{0,+}^2$, is equivalent to the dielectric CR time, $2\tau_G^{CR} \simeq 14.6$ s (cf. Appendix C) and thus all retardation times, $N_o^2\zeta_{CR}/\kappa\lambda_{k,\alpha}^2$ and $N_o^2\zeta_{CR}/\kappa\xi_k^2$, can be estimated from this $2\tau_G^{CR}$ value and the known $\lambda_{k,\alpha}/\lambda_{0,+}$ and $\xi_k/\lambda_{0,+}$ ratios (cf. eqs B8 and B10). Hence, all time-dependent terms included in eqs B27–B29 can be specified experimentally.

The top panel of Figure 10 shows the square displacements $\langle \mathbf{D}_i^2\rangle$, $\langle \mathbf{D}_i\cdot\mathbf{D}_{oj}\rangle$, and $\langle \mathbf{D}_{o1}\cdot\mathbf{D}_{o2}\rangle$ normalized by the equilibrium end-to-end distance of the outer arm, $N_o a^2$. All of these normalized displacements increase with t. More importantly, $\langle \mathbf{D}_i\cdot\mathbf{D}_{oj}\rangle$ (square) and $\langle \mathbf{D}_{o1}\cdot\mathbf{D}_{o2}\rangle$ (circle) are very small in a quite wide range of $t < 0.6t^*$ and approach $\langle \mathbf{D}_i^2\rangle$ (asterisk) only in the vicinity of t^*. This result indicates that the cross-correlation between the entanglement segments on the surviving tube edge and the branching/bifurcation point as well as between the two segments on the different edges emerges significantly only at $t > 0.6t^*$ where the tube edge came into the close vicinity of the branching/bifurcation point. (At $t > 0.6t^*$, the index of the segment on the tube edge, $N_o\varphi_o'$, decreased well below $0.1N_o$; cf. filled triangles in Figure 5.)

This behavior of the cross-correlation is most clearly seen in the bottom panel Figure 10 where $Q_{oi}(t) \equiv \langle \mathbf{D}_i\cdot\mathbf{D}_{oj}\rangle/\langle \mathbf{D}_i^2\rangle$ and $Q_{oo}(t) \equiv \langle \mathbf{D}_{o1}\cdot\mathbf{D}_{o2}\rangle/\langle \mathbf{D}_i^2\rangle$ are plotted against t. $Q_{oi}(t)$ and $Q_{oo}(t)$ are very close to zero at $t < 0.6t^*$ and rapidly increase to unity with increasing t in a range of t between $0.6t^*$ and t^*. We also note $Q_{oi}(t) \ge Q_{oo}(t)$ in the entire range of $t \le t^*$ (because the contour distance between the two segments involved is smaller for $Q_{oi}(t)$ than for $Q_{oo}(t)$). These $Q_{oi}(t)$ and $Q_{oo}(t)$ are utilized in the evaluation of $\varphi'(t)$ for the test of DTD picture.

It should be noted that the above feature of the cross-correlation is expected for the actual CR dynamics of the CT-PI chain, i.e., even if this dynamics has a non-Rouse feature. Thus, in general, the functions $Q_{oi}(t)$ and $Q_{oo}(t)$ are considered to be the increasing function of t, satisfying the relationships $Q_{oi}(t) \ge Q_{oo}(t)$ at $t < t^*$ and $Q_{oi}(t^*) = Q_{oo}(t^*) = 1$.

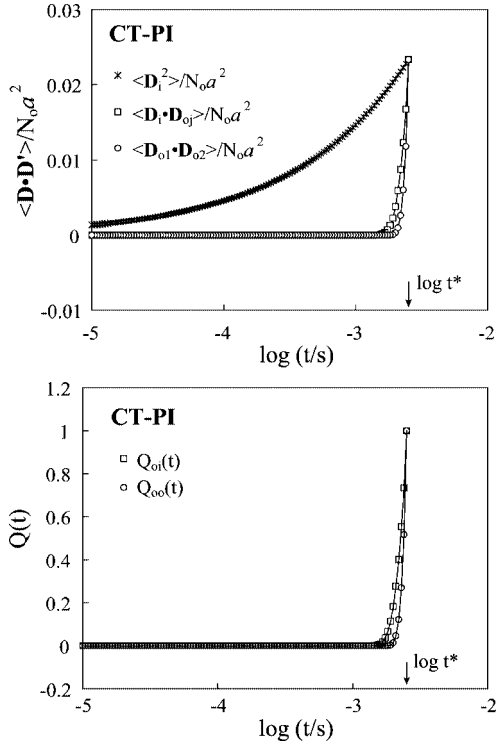

Figure 10. Top panel: normalized square displacements $\langle \mathbf{D}_i^2 \rangle$ (asterisk), $\langle \mathbf{D}_i \cdot \mathbf{D}_{oj} \rangle$ (square), and $\langle \mathbf{D}_{o1} \cdot \mathbf{D}_{o2} \rangle$ (circle) obtained from Rouse-CR analysis. For further details, see Appendix B. Bottom panel: plots of $Q_{oi}(t) \equiv \langle \mathbf{D}_i \cdot \mathbf{D}_{oj} \rangle / \langle \mathbf{D}_i^2 \rangle$ and $Q_{oo}(t) \equiv \langle \mathbf{D}_{o1} \cdot \mathbf{D}_{o2} \rangle / \langle \mathbf{D}_i^2 \rangle$ against t.

B.3. Normalized Stress Decay Function. For the tethered/bifurcated chain subjected to a small step shear strain γ at $t = 0$, the shear stress $\sigma(t)$ at $t > 0$ is related to the chain conformation as[3,4]

$$\sigma(t) = \kappa \nu \sum_{j=1}^{3} \int \left\langle \frac{\partial \mathbf{r}^{[j]}(n,t)}{\partial n} \frac{\partial \mathbf{r}^{[j]}(n,t)}{\partial n} \right\rangle_{xy} \mathrm{d}n \qquad \text{(B30)}$$

where κ ($= 3k_BT/a^2$) is the spring constant, ν is the number of chains per unit volume, and x and y indicate the shear and shear-gradient directions, respectively. The integral is conducted for all segments of the chain.

As noted from eqs B6, B7, and B30, $\sigma(t)$ is expressed as a sum of the xy components of the dyadic averages of the eigenmode amplitudes. Considering that the chain is fully equilibrated at $t < 0$ and affinely deformed at $t = 0$, we can calculate these components at $t = 0$ with the aid of eqs B21–B24: $\langle \mathbf{A}_p^{[j]}(0) \mathbf{A}_q^{[j]}(0) \rangle_{xy} = 2\delta_{pq} N_o a^2 \gamma / 5\xi_p^2$, $\langle \mathbf{A}_p^{[1]}(0) \mathbf{A}_q^{[2]}(0) \rangle_{xy} = -4\delta_{pq} N_o a^2 \gamma / 15\xi_p^2$, $\langle \mathbf{A}_p(0) \mathbf{B}_{q,\beta}(0) \rangle_{xy} = 0$, and $\langle \mathbf{B}_{p,\alpha}(0) \mathbf{B}_{q,\beta}(0) \rangle_{xy} = \delta_{pq} \delta_{\alpha\beta} N_o a^2 \gamma / 5\lambda_{p,\alpha}^2$. Combining these initial conditions with the general expressions of $\mathbf{A}_k^{[j]}(t)$ and $\mathbf{B}_{k,\alpha}(t)$ given by eqs B15 and B16, we can readily calculate $\sigma(t)$. The result can be summarized as the normalized stress decay function $\psi(t)$ ($= 1$ at $t = 0$):

$$\psi(t) = \frac{1}{4N_o} \sum_{k=0}^{N_o-1} \left\{ 2 \exp\left(-\frac{2\kappa \xi_k^{\,2}}{N_o^{\,2} \zeta_{CR}} t \right) + \exp\left(-\frac{2\kappa \lambda_{k,+}^{\,2}}{N_o^{\,2} \zeta_{CR}} t \right) + \exp\left(-\frac{2\kappa \lambda_{k,-}^{\,2}}{N_o^{\,2} \zeta_{CR}} t \right) \right\} \qquad \text{(B31)}$$

The front factor of 2 appearing in the first term in the right-hand side results from the dual degeneracy of the A modes (having the node at the bifurcation point). Taking the longest relaxation time, $N_o^2 \zeta_{CR} / 2\kappa \lambda_{0,+}^2$, to be identical to $2\tau_G^{CR}$ and considering a contribution from the intrinsic Rouse fluctuation to $\psi_{CR}(t)$, we obtain eq 10 in the text: The relaxation rate coefficient r_p appearing in eq 10 coincides with the ratios, $(\lambda_{k,+}/\lambda_{0,+})^2$ for $p = 4k + 1$ (= multiple of 4 plus 1), $(\xi_k/\lambda_{0,+})^2$ for $p = 4k + 2$ and $4k + 3$ (= multiple of 4 plus 2 or 3), and $(\lambda_{k,-}/\lambda_{0,+})^2$ for $p = 4k + 4$ (= multiple of 4) with $k \geq 0$. In eq 10, we have treated the degenerated series of A modes separately (by indexing them with $p = 4k + 2$ and $4k + 3$; cf. eq 11b) and assigned the same coefficient r_p to them.

Appendix C. Estimation of CR Time for CT-PI

Comparing eqs 10 and B31, we note that the CR time $2\tau_G^{CR}$ for CT-PI appearing in eq 10 is expressed as

$$2\tau_G^{CR} = \frac{\zeta_{CR}^{CT-PI}}{2\kappa} \left(\frac{N_o}{\theta} \right)^2 \quad \text{with } \theta = \sin^{-1}\left(\frac{1}{\sqrt{6}} \right) \qquad \text{(C1)}$$

Here, κ ($= 3k_BT/a^2$) is the spring strength and ζ_{CR}^{CT-PI} denotes an *effective* friction coefficient of the entanglement segment of CT-PI: κ is independent of motion of surrounding chains, while ζ_{CR}^{CT-PI} increases on slowing of this motion. For a tethered linear Rouse chain composed of N' segments (and having the molecular weight M_{arm}; a model for an arm of star PI), $2\tau_G^{CR}$ is similarly expressed as

$$2\tau_G^{CR} = \frac{\zeta_{CR}^{star-PI}}{2\kappa} \left\{ \frac{N'}{(\pi/2)} \right\}^2 \qquad \text{(C2)}$$

with $\zeta_{CR}^{star-PI}$ being the effective friction coefficient of the entanglement segment of star PI. For monodisperse star PI,[10,41] the viscoelastic and dielectric data suggest that $\zeta_{CR}^{star-PI}$ is almost proportional to the dielectric relaxation time $<\tau_\epsilon>_w$ (shown in Figure 6 with unfilled squares). Within the context of Rouse-CR model, the same proportionality is expected for CT-PI. Then, from eqs C1 and C2, we obtain an estimate of τ_G^{CR} for CT-PI

$$\tau_G^{CR}(\text{CT-PI}) = \left\{ \frac{\pi/2}{\theta} \right\}^2 \left\{ \frac{M_o}{M_{arm}} \right\}^2 \left\{ \frac{\langle \tau_\epsilon \rangle_w(\text{CT-PI})}{\langle \tau_\epsilon \rangle_w(\text{star-PI})} \right\} \tau_G^{CR}(\text{star-PI}) \qquad \text{(C3)}$$

In eq C3, the segment number ratio N_o/N' (with N_o and N' coming from eqs C1 and C2, respectively) has been replaced by the molecular weight ratio M_o/M_{arm} so that τ_G^{CR} is estimated without being affected by our choice of the N_o value ($N_o = 2$ or 3). For a star PI with $M_{arm} = 40.7 \times 10^3$ ($\simeq M_{span}/2$ for our CT-PI), experiments gave $\langle \tau_\epsilon \rangle_w = 0.26$ s and $\tau_G^{CR} = 1.5$ s at 40 °C.[41] Utilizing these τ data and the $\langle \tau_\epsilon \rangle_w$ data for CT-PI ($\langle \tau_\epsilon \rangle_w = 1.0$ s; cf. Figure 6) in eq C3, we obtain the estimate, $\tau_G^{CR} \simeq 7.3$ s for CT-PI. (This estimate did not change significantly even when the τ data for other star-PI[41] were utilized in eq C3.)

References and Notes

(1) Doi, M.; Edwards, S. F. *The Theory of Polymer Dynamics*; Clarendon: Oxford, 1986; p 239.
(2) Graessley, W. W. *Adv. Polym. Sci.* **1982**, *47*, 67–117.
(3) Watanabe, H. *Prog. Polym. Sci.* **1999**, *24*, 1253–1403.
(4) McLeish, T. C. B. *Adv. Phys.* **2002**, *51*, 1379–1527.
(5) Graham, R. S.; Likhtman, A. E.; McLeish, T. C. B. *J. Rheol.* **2003**, *47*, 1171–1200.
(6) Nair, D. M.; Schieber, J. D. *Macromolecules* **2006**, *39*, 3386–3397.
(7) Tasaki, H.; Takimoto, J.; Doi, M. *Comput. Phys. Commun.* **2001**, *142*, 136–139.
(8) Masubuchi, Y.; Inanniruberto, G.; Greco, F.; Marrucci, G. *Rheol. Acta* **2006**, *46*, 297–303.
(9) Watanabe, H.; Ishida, S.; Matsumiya, Y.; Inoue, T. *Macromolecules* **2004**, *37*, 6619–6631.
(10) Watanabe, H.; Sawada, T.; Matsumiya, Y. *Macromolecules* **2006**, *39*, 2553–2561.
(11) Watanabe, H.; Ishida, S.; Matsumiya, Y.; Inoue, T. *Macromolecules* **2004**, *37*, 1937–1951.
(12) Marrucci, G. *J. Polym. Sci., Phys. Ed.* **1985**, *23*, 159–177.
(13) Ball, R. C.; McLeish, T. C. B. *Macromolecules* **1989**, *22*, 1911–1913.

(14) Milner, S. T.; McLeish, T. C. B. *Macromolecules* **1997**, *30*, 2159−2166; **1998**, *31*, 7479−7482.
(15) Matsumiya, Y.; Watanabe, H.; Osaki, K. *Macromolecules* **2000**, *33*, 499–506.
(16) Watanabe, H.; Matsumiya, Y.; Inoue, T. *Macromolecules* **2002**, *35*, 2339–2357.
(17) Watanabe, H.; Matsumiya, Y.; Osaki, K. *J. Polym. Sci., Part B: Polym. Phys.* **2000**, *38*, 1024–1036.
(18) Matsumiya, Y.; Watanabe, H. *Macromolecules* **2001**, *34*, 5702–5710.
(19) Roovers, J.; Toporowski, P. M. *Macromolecules* **1987**, *20*, 2300–2306.
(20) Kapnistos, M.; Vlassopoulos, D.; Roovers, J.; Leal, L. G. *Macromolecules* **2005**, *38*, 7852–7862.
(21) Inkson, N. J.; Graham, R. S.; McLeish, T. C. B.; Groves, D. J.; Fernyhough, C. M. *Macromolecules* **2006**, *39*, 4217–4227.
(22) Roovers, J. *Macromolecules* **1984**, *17*, 1196–1200.
(23) Archer, L. A.; Varshney, S. K. *Macromolecules* **1998**, *31*, 6348–6355.
(24) McLeish, T. C. B.; Allgaier, J.; Bick, D. K.; Bishko, G.; Biswas, P.; Blackwell, R.; Blottiere, B.; Clarke, N.; Gibbs, B.; Groves, D. J.; Hakiki, A.; Heenan, R. K.; Johnson, J. M.; Kant, R.; Read, D. J.; Young, R. N. *Macromolecules* **1999**, *32*, 6734–6758.
(25) McLeish, T. C. B.; Larson, R. G. *J. Rheol.* **1998**, *42*, 81–110.
(26) Archer, L. A.; Juliani, *Macromolecules* **2004**, *37*, 1076–1088.
(27) Dorgan, J. R.; Knauss, D. M.; Al-Muallum, H. A.; Huang, T.; Vlassopoulos, D. *Macromolecules* **2003**, *36*, 380–388.
(28) Blackwell, R. J.; Harlen, O. G.; McLeish, T. C. B. *Macromolecules* **2001**, *34*, 2579–2596.
(29) (a) van Ruymbeke, E.; Orfanou, K.; Kapnistos, M.; Iatrou, H.; Pitsikalis, M.; Hadjichristidis, N.; Lohse, D. J.; Vlassopoulos, D. *Macromolecules* **2007**, *40*, 5941–5952. (b) van Ruymbeke, E.; Keunings, R.; Bailly, C. *J. Non-Newtonian Fluid Mech.* **2005**, *128*, 7–22.
(30) (a) It is very important to test molecular models against different types of dynamic properties. For example, the full-DTD models can describe the viscoelastic property of star chains but cannot consistently describe the diffusion[30b] and dielectric[16] data of the same chains. (b) Frischknecht, A. L.; Milner, S. T. *Macromolecules* **2000**, *33*, 9764–9768.
(31) Park, S. J.; Shanbhag, S.; Larson, R. G. *Rheol. Acta* **2005**, *44*, 319–330.
(32) Chalari, I.; Hadjichristidis, N. *J. Polym. Sci., Polym. Chem.* **2002**, *40*, 1519–1526.
(33) Graessley, W. W. *Adv. Polym. Sci.* **1974**, *16*, 1–179.
(34) Imanishi, Y.; Adachi, K.; Kotaka, T. *J. Chem. Phys.* **1988**, *89*, 7585–7592.
(35) Fetters, L. J.; Kiss, A. D.; Pearson, D. S.; Quack, G. F.; Vitus, F. J. *Macromolecules* **1993**, *26*, 647–654.
(36) Watanabe, H. *Macromol. Rapid Commun.* **2001**, *22*, 127–175.
(37) Watanabe, H. *Korean-Australian Rheol. J.* **2001**, *13*, 205–217.
(38) van Ruymbeke E.; Vlassopoulos, D.; Hadjichristidis, N.; Watanabe, H., manuscript in preparation.
(39) The M_e value ($= 5 \times 10^3$ for PI[33]) is obtained from a standard/classical expression of the entanglement plateau modulus, $G_N = \rho RT/M_e$. This value becomes smaller if we adopt the Doi−Edwards expression of G_N ($= 4\rho RT/5M_e$).[3,4] However, this paper attempts to examine the DTD picture experimentally by minimizing the reliance on detailed/delicate assumptions in particular molecular models. Following this strategy, this paper utilizes the standard/classical M_e value as a base for evaluation of N_i and N_o.
(40) For both of the full- and partial-DTD cases, the survival fraction $\varphi'(t)$ of the dilated tube is almost indistinguishable from the dielectric $\Phi(t)$ data in a considerably wide range of t where the second terms of eqs 8 and 9, representing the effect of the arm displacement at the dilated tube edge, are negligibly small compared to $\Phi(t)$. However, these terms become non-negligible at the long-time end of the relaxation and $\varphi'(t)$ becomes moderately larger than $\Phi(t)$ at those t; see asterisks and squares in Figure 5.
(41) Qiao, X.; Sawada, T.; Matsumiya, Y.; Watanabe, H. *Macromolecules* **2006**, *39*, 7333–7341.
(42) Sawada, T.; Qiao, X.; Watanabe, H. *Nihon Reoroji Gakkaishi* (*J. Soc. Rheol. Jpn.*) **2007**, *35*, 11–20.
(43) Watanabe, H.; Urakawa, O.; Kotaka, T. *Macromolecules* **1994**, *27*, 3525–3536.
(44) Watanabe, H.; Yamada, H.; Urakawa, O. *Macromolecules* **1995**, *28*, 6443–6453.
(45) Zimm, B. H.; Kilb, R. W. *J. Polym. Sci.* **1959**, *37*, 19–42.

MA800503E